University of Utrecht

Debye Institute

Quantum Nano-photonics Group

Self-Scattering of Gold Nano-particles under Femtosecond Laser Ablation Conditions

Author:
Gordian Zomer BSc

Supervisor:
Dr. Dries van Oosten

July 14, 2016

Abstract

This thesis covers the interaction of a femtosecond pulsed laser (about $150\,\mathrm{fs}$ at FWHM) with spherical gold nano-particles ($100\,\mathrm{nm}$ in diameter) in the ablation regime. The study is separated into an experimental part and a simulation part.

For the experimental part, gold nano-particles are isolated by the drop casting technique on a substrate. Scanning electron microscope data is used as a mapping system for our diffraction limited optical ablation setup. The self-scattering of the nano-particles as a function of fluence is investigated. We found the ablation threshold to be about $0.03\,\mathrm{J\,cm^{-2}}$ and reached a maximum fluence of about $0.2\,\mathrm{J\,cm^{-2}}$. The self-scattering results from ablated nano-particles are inconclusive due to a high background contribution from the substrate.

The simulation part covers the light scattering properties of gold nano-particles sized around the Rayleigh limit. Due to high electron temperatures reached (2/3 of the Fermi temperature for gold) in femtosecond laser-gold interaction, we incorporate *ab initio* data by Lin and Zhigilei on the electron heat capacity into our model. We also include experimental data by Fourment et al. on the number of free conduction electrons per atom. Results show a decrease in reflectivity during irradiation at a fluence of $0.8\,\mathrm{J\,cm^{-2}}$. The model allows to go up to a fluence of $10\,\mathrm{J\,cm^{-2}}$, where we observe a decrease in reflectivity of about $10\,\%$.

Contents

1 Introduction

The invention of the laser by Theodore Maiman in 1960 heralded a new age of physics research and material processing. Today, the field of laser application is enormous. They include communication, medicine, laser cutting and nano-fabrication.

Advances in the last two decades on lasers with ultrashort pulse durations paved the way to study materials on ultrashort timescales. Pulse durations in the order of femtoseconds (10^{-15} s) can now be reached easily with corresponding intensities on the order of 10^{14} W cm^{-2}. Illuminating matter with these short pulses and high intensities can induce interesting non-linear behaviour without melting the lattice while the laser pulse is still present. After the pulse, the irradiated material will vaporize due to extreme heating in a process called ablation. [1]

In this thesis the interaction of fs-laser pulses with gold nano-particles is studied. This is done by investigating the change in reflectivity of the gold particles during irradiation using different laser fluences above ablation threshold. An observable change in reflectivity allows to study the processes at work during ablation.

Laser-gold interaction has been modeled before using CPU resource intensive finite difference time domain (FDTD) simulations [2]. For spherical particles Mie theory can be used. It is less resource intensive but mathematically very complex. For particles that are small enough with respect to the wavelength of the incoming electromagnetic field, we can apply Rayleigh theory. The latter has been done and it has provided a simple model that can be verified by future experiments.

The theory necessary to understand the laser-gold interactions will be explained in chapter 2. Chapters 3 and 4 cover a gold nano-particle ablation experiment and a laser-gold nano-particle simulation, respectively.

2 Theory

In this section we will discuss the most relevant processes in laser-gold interaction on femtosecond timescales. Basically, only the electrons in the conduction band will interact with such short laser pulses. They will heat up, which extremely alters their collision rate. This collision rate then affects the dielectric function, which governs the scattering and absorption of the laser pulse incident on a small gold particle.

2.1 Femtosecond Laser Excitation Timescales

For a femtosecond laser pulse irradiating a solid, the laser only interacts with the material on a femtosecond timescale. The irradiation can lead to material removal or ablation if the pulse intensity is high enough. During ultrashort laser pulses, the processes that lead to ablation are temporally separated.

For conductors, such as gold, the laser energy is first deposited onto the conduction electrons, which leads to electron excitation. This first step towards ablation takes place within the duration of the pulse. Next is electron-lattice heating, which takes about a picosecond. This is followed by melting of the lattice, which takes several picoseconds. The consecutive material removal can take up to several nanoseconds. [3]

In conclusion, an ultrashort laser pulse interacts with the conduction electrons while leaving the lattice at rest on sub-ps timescales. This means that we only need to concern ourselves with the electron properties and we can consider the lattice as stable.

2.2 Drude Model

The interaction between metals and electromagnetic radiation is mostly due to free conduction electrons in metals. To study how those electrons behave, we use the Drude-Sommerfeld model for a free electron gas. This model works well for metals in the infrared regime in which our experiments and simulations are done. We do not need to supplement it with interband transitions, because they become dominant only below $\sim 550\,\text{nm}$ for gold. The equation of motion for the Drude model is given by

$$m_\text{e}\frac{\partial^2 \mathbf{r}}{\partial t^2} + m_\text{e}\nu_\text{e}\frac{\partial \mathbf{r}}{\partial t} = e\mathbf{E}_0 \text{e}^{-i\omega t} , \tag{2.1}$$

with e and m_e the electron charge and mass, $\mathbf{r}$ the displacement of an electron due to the presence of an electric field $\mathbf{E}_0$, oscillating with frequency ω and with a collision

frequency

$$\nu_{\mathrm{e}} = v_{\mathrm{F}}/l \, ,$$

where v_{F} is the Fermi velocity and l is the mean free path between collisions. This can be written as $\nu_{\mathrm{e}} = 1/\tau$, in which case τ is the mean time between collisions or the Drude damping time. We then substitute $\mathbf{r} = \mathbf{r}_0 e^{-i\omega t}$ in Eq. (2.1) and obtain

$$\mathbf{r} = \frac{-e\mathbf{E}_0 e^{-i\omega t}}{m_{\mathrm{e}}(\omega^2 + i\frac{\omega}{\tau})} \, .$$

From Maxwells equations we know that the electric current density

$$\mathbf{j} = \sigma \mathbf{E} \, , \tag{2.2}$$

with σ the electric conductivity. This quantity can also be written as

$$\mathbf{j} = -Ne\frac{\partial \mathbf{r}}{\partial t} \, , \tag{2.3}$$

where N is the number of free electrons per unit volume. From Eq. (2.2) and Eq. (2.3) we obtain the electric conductivity

$$\sigma(\omega) = \frac{Ne^2}{m_{\mathrm{e}}} \frac{i\omega}{(\omega^2 + i\frac{\omega}{\tau})} \, . \tag{2.4}$$

The electric conductivity leads to the dielectric function [2]

$$\varepsilon(\omega) = 1 + \frac{i\sigma(\omega)}{\varepsilon_0 \omega} \, . \tag{2.5}$$

From this we obtain the dielectric function for the Drude model

$$\varepsilon_{\mathrm{Drude}}(\omega) = 1 - \frac{\omega_{\mathrm{p}}^2}{\omega^2 + i\frac{\omega}{\tau}} \, , \tag{2.6}$$

with

$$\omega_{\mathrm{p}} = \sqrt{\frac{Ne^2}{m_{\mathrm{e}}\varepsilon_0}} \tag{2.7}$$

the free electron or plasma oscillation frequency. To better reproduce experimental data, one has to introduce a constant offset $\varepsilon_\infty = 6.0$ to Eq. (2.6) [4]. This offset accounts for higher-energy interband transitions, which are not considered in the Drude model.

3

2.3 Electron Collision Frequency

For Fermi liquids, it is known that the electron collision frequency goes as $\nu_e \propto T_e^2$ when $T_e \ll T_F$, with T_e the electron temperature and T_F the Fermi temperature, which is $64\,000\,\text{K}$ for gold. This scaling is a consequence of the electron degeneracy at low temperatures. Fourment *et al.* [5] found that the behaviour of the electron collision frequency deviates significantly from the Fermi liquid temperature scaling when approaching the Fermi temperature. This is due to the increase in conduction electrons by thermal excitations from the d-band. Their experiments determined the electron collision frequency and conduction electron density as a function of the electron temperature T_e in the range of 0.6-5 eV, corresponding to 7000-58 000 K. From this they proposed a heuristic model for the electron collision frequency ν_e^d due to d-band collisions

$$\nu_e^d = A(11 - Z_{\text{eff}})(Z_{\text{eff}} - 1) \,,$$

with Z_{eff} the effective number of conduction electrons per atom and $A = 0.36\,\text{fs}^{-1}$. We then find for the Drude damping time

$$\tau = \frac{1}{\nu_{\text{ph}} + \nu_e^d} = \frac{1}{\nu_{\text{ph}} + A(11 - Z_{\text{eff}})(Z_{\text{eff}} - 1)} \,, \tag{2.8}$$

where $\nu_{\text{ph}} = 0.129\,\text{fs}^{-1}$ is due to the electron-phonon collisions in gold. This value is constant in our model, because the electron-electron collisions dominate in the timescale and temperature range considered [5].

2.4 Electron Heating

Since the electron collision frequency ν_e depends on the electron temperature (through Z_{eff}) we need to calculate the change in electron temperature during a femtosecond pulse. Here we can safely neglect the electron-lattice heating, because that occurs in the order of a picosecond. To model the increase in electron temperature, we apply the simplified heat equation from [6], where we have omitted the position dependence since we are considering small particles

$$C_e \frac{\partial [T_e(t)]}{\partial t} = \frac{\sigma_{\text{abs}}}{V} I(t) \,, \tag{2.9}$$

with C_e the electron specific heat capacity, T_e the electron temperature, σ_{abs} the absorption cross-section, V the volume of the particle and I the laser intensity. These values will be specified in Sec. (4).
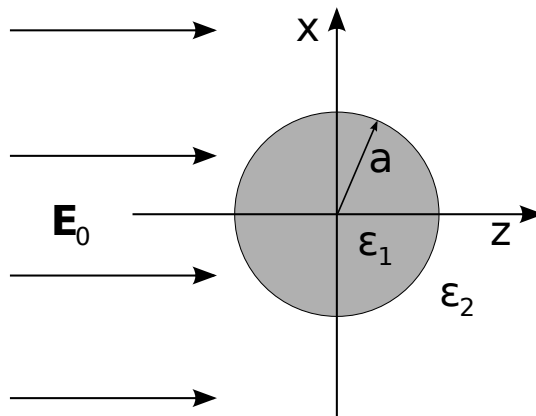
Figure 2.1: Small conducting sphere under influence of an electric field $\mathbf{E}_0$.

2.5 Scattering and Absorption of a Small Sphere

We consider a small conducting sphere of radius a and dielectric constant ε_1 in a medium with dielectric constant ε_2 and an electric field propagating in the $\mathbf{z}$-direction. This situation is sketched in Fig. (2.1). The electric field can be represented by a potential

$$\mathbf{E} = -\nabla V \, ,$$

which must satisfy the Laplace equation

$$\nabla^2 V = 0 \tag{2.10}$$

and the appropriate boundary conditions between adjacent materials. In spherical coordinates (r, θ, φ), the Laplace equation is given as

$$\frac{1}{r^2 \sin\theta} \left[\sin\theta \frac{\partial}{\partial r} \left(r^2 \frac{\partial}{\partial r} \right) + \frac{\partial}{\partial r} \left(\sin\theta \frac{\partial}{\partial \theta} \right) + \frac{1}{\sin\theta} \frac{\partial^2}{\partial \varphi^2} \right] V(r, \theta, \varphi) = 0 \, . \tag{2.11}$$

The continuity of the electric fields imply the following boundary conditions

$$\begin{aligned} [V_1]_{r=a} &= [V_2]_{r=a} \, , \\ \left[\frac{\partial V_1}{\partial \theta} \right]_{r=a} &= \left[\frac{\partial V_2}{\partial \theta} \right]_{r=a} \, , \\ \varepsilon_1 \left[\frac{\partial V_1}{\partial r} \right]_{r=a} &= \varepsilon_2 \left[\frac{\partial V_2}{\partial r} \right]_{r=a} \, , \end{aligned} \tag{2.12}$$

where V_1 is the potential inside the sphere. Outside the sphere, the potential V_2 consists of the potentials of the incoming and scattered fields $V_2 = V_{\text{scatter}} + V_0$. The incoming field is directed along the **z**-direction $\mathbf{E} = E_0\hat{\mathbf{z}}$, so $V_0 = -E_0 r \cos\theta$. After applying the boundary conditions we obtain the potentials inside and outside the sphere

$$V_1 = -E_0 \frac{3\varepsilon_2}{\varepsilon_1 + 2\varepsilon_2} r \cos\theta \,,$$

$$V_2 = -E_0 r \cos\theta + E_0 \frac{\varepsilon_1 - \varepsilon_2}{\varepsilon_1 + 2\varepsilon_2} a^3 \frac{\cos\theta}{r^2} \,.$$

Using $\mathbf{E} = -\nabla V$ we calculate the electric fields inside and outside the sphere

$$\mathbf{E}_1 = E_0 \frac{3\varepsilon_2}{\varepsilon_1 + 2\varepsilon_2} \hat{\mathbf{z}} \,,$$

$$\mathbf{E}_2 = E_0 (\cos\theta \hat{\mathbf{r}} - \sin\theta \hat{\boldsymbol{\theta}}) + \frac{\varepsilon_1 - \varepsilon_2}{\varepsilon_1 + 2\varepsilon_2} \frac{a^3}{r^3} E_0 (2\cos\theta \hat{\mathbf{r}} + \sin\theta \hat{\boldsymbol{\theta}}) \,. \qquad (2.13)$$

If the sphere is small enough, we can approximate its electric field as a dipole. The potential for an ideal dipole, with **p** the dipole moment, is given as

$$V_{\text{dip}} = \frac{\mathbf{p} \cdot \hat{\mathbf{r}}}{4\pi\varepsilon_0\varepsilon_2 r^2} = \frac{p\cos\theta}{4\pi\varepsilon_0\varepsilon_2 r^2} \,,$$

which yields the following dipole field, expressed in spherical coordinates

$$\mathbf{E}_{\text{dip}} = \frac{p}{4\pi\varepsilon_0\varepsilon_2 r^3} (2\cos\theta \hat{\mathbf{r}} + \sin\theta \hat{\boldsymbol{\theta}}) \,. \qquad (2.14)$$

The second term in Eq. (2.13) is equal to the electric field of a dipole located at the center of the sphere, which results in the dipole moment **p** induced by the external field $\mathbf{E}_0$ [4]

$$\mathbf{p} = 4\pi\varepsilon_0 a^3 \frac{\varepsilon_1 - \varepsilon_2}{\varepsilon_1 + 2\varepsilon_2} \varepsilon_2 \mathbf{E}_0 \,.$$

The polarizability α of the sphere is defined as

$$\mathbf{p} = \varepsilon_2 \alpha \mathbf{E}_0 \,,$$

$$\alpha = 4\pi\varepsilon_0 a^3 \frac{\varepsilon_1 - \varepsilon_2}{\varepsilon_1 + 2\varepsilon_2} \; . \tag{2.15}$$

The scattering cross-section of the sphere is obtained by dividing the radiated power of the sphere by the intensity of the incoming field. The average radiated power $\langle P_{\text{rad}} \rangle$ for a dipole and the average intensity $\langle I \rangle$ of a plane wave are given by

$$\langle P_{\text{rad}} \rangle = \frac{|\mathbf{p}|^2}{4\pi\varepsilon_0\varepsilon_2} \frac{n^3\omega^4}{3c^3} \; ,$$
$$\langle I \rangle = \frac{cn\varepsilon_0}{2} |E_0|^2 \; ,$$

with n the refractive index of the medium, ω the angular frequency of the field and c the speed of light. Dividing these yields the scattering cross-section

$$\sigma_{\text{scat}} = \frac{\langle P_{\text{rad}} \rangle}{\langle I \rangle} = \frac{k^4}{6\pi\varepsilon_0^2} |\alpha|^2 \; , \tag{2.16}$$

where we have used that $\omega = \frac{kc}{n}$ and $n = \sqrt{\varepsilon_2}$.

The sphere not only scatters the incident field, but it also absorbs power. The power absorbed by a dipole is determined as

$$\langle P_{\text{abs}} \rangle = \frac{\omega}{2}\text{Im}(\mathbf{p} \cdot \mathbf{E}_0^*) \; ,$$

from which we obtain the following absorption cross-section

$$\sigma_{\text{abs}} = \frac{\langle P_{\text{abs}} \rangle}{\langle I \rangle} = \frac{k}{\varepsilon_0}\text{Im}(\alpha) \; . \tag{2.17}$$

3 Experiment

To perform ablation experiments on gold nano-particles, they are first deposited onto a glass substrate with a 60 nm conductive layer of Indium Tin Oxide (ITO). The conductive layer is used to prevent the build-up of charge when imaging with a scanning electron microscope (SEM). The SEM images are used to provide a mapping system for the optical images, because the size of the gold nano-particles is below the diffraction limit of our setup and therefore single gold particles can not directly be distinguished from clusters of gold particles. After the mapping process a suitable gold nano-particle is selected for ablation. The ablation procedure is then followed by data analysis in which the self-scattering of the particle during the laser pulse is investigated.

3.1 Drop Casting Technique

Drop casting is often used in the process of spin-coating of particles onto a substrate. Here we use it without spin-coating and just use the *coffee ring effect* of a drying fluid. This effect is demonstrated in Fig. (3.1), where (nano-)particles are initially homogeneously distributed across the droplet and end up mostly on the sides. We want to use this effect to ensure that there are single gold nano-particles, sufficiently separated, near the center of the droplets.
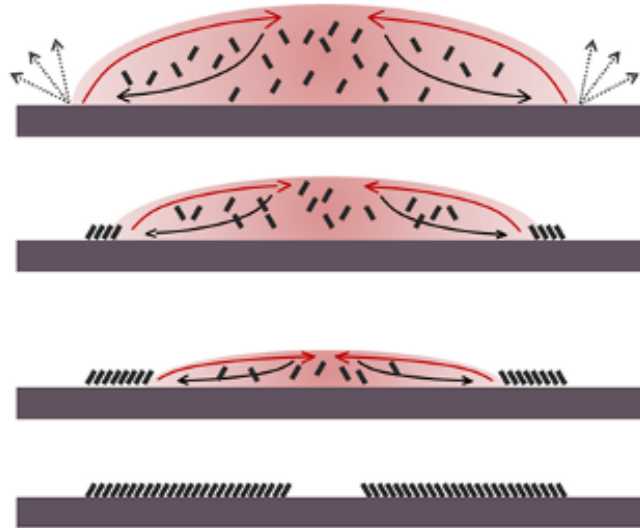

Figure 3.1: Drop casting method. The droplet evaporates faster at the droplet-air-substrate interface, which creates an edgeward flow inside the droplet. This will result in a higher density of deposited particles at the edges than at the center. Image taken from [7].

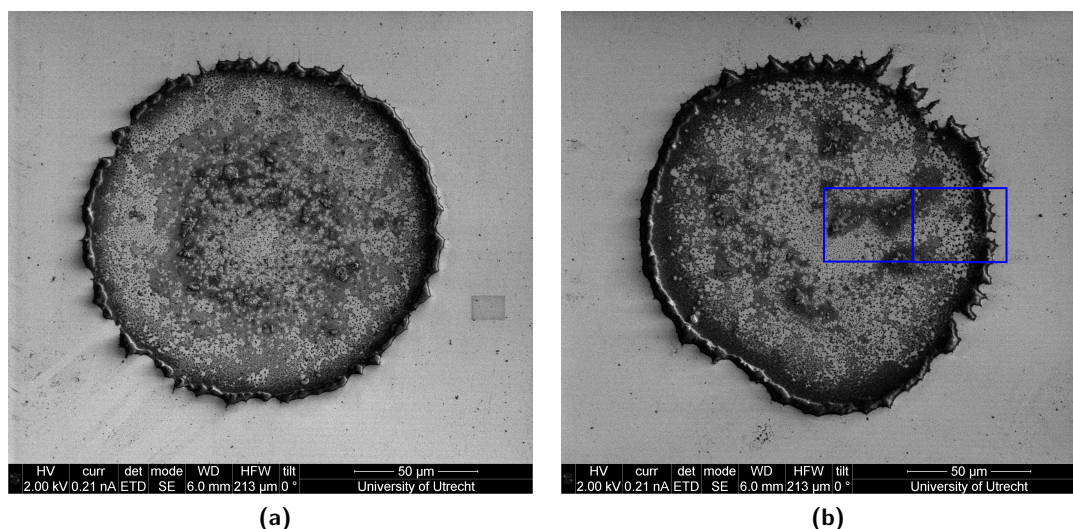The gold nano-particles (diameter $d = 100 \pm 5$ nm, corresponding to roughly 400

Figure 3.2: Overview of two dropcasted droplets, with a diameter of about $150\,\mu m$, as seen under a scanning electron microscope. The blue rectangles in (b) are zoomed in upon in Fig. (3.3).

million atoms) are dispersed in water with a concentration of $0.05\,\mathrm{mg\,mL^{-1}}$. From this solution $1\,\mathrm{mL}$ is taken with a syringe and diluted with $9\,\mathrm{mL}$ of ethanol. This new solution is then sonicated for fifteen minutes to deagglomerate clusters of nano-particles. To prepare the ITO coated glass for dropcasting, it is first cleaned with acetone, then with isopropanol and lastly sonicated in ethanol. After the preparation of the solution and the substrate, the droplets are carefully deposited with a syringe on the ITO layer. The mean diameter of the droplets is about $0.5\,\mathrm{mm}$ before drying.

An overview of two dried up dropcasted droplets is shown in Fig. (3.2) as seen under a SEM. One of the most striking features are the dark, coffee ring like, rims which contain a high amount of clustered gold nano-particles, dust and contaminants from the solution. Inside the ring are some irregularly shaped dust particles and the centers seem relatively clean.

At this zoom level however, gold nano-particles are about be the size of a single pixel. Zoomed in versions of the blue frames of Fig. (3.2b) are given in Fig. (3.3). The cropped Figs. (3.3c and 3.3d) clearly show gold nano-particles as small bright dots. The gold nano-particles in Fig. (3.3d) are closer to each other and often form larger aggregates when compared to Fig. (3.3c), because Figs. (3.3b and 3.3d) were taken closer to the rim. At this level of detail it is also clearly visible that the black rims in the two overview pictures are in fact filled with large clumps of gold particles.
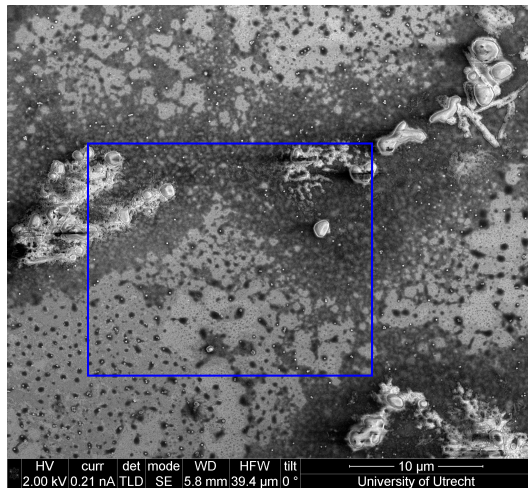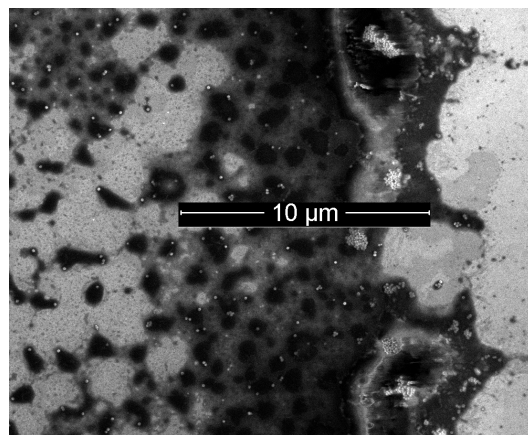
(a) Zoomed in on center.
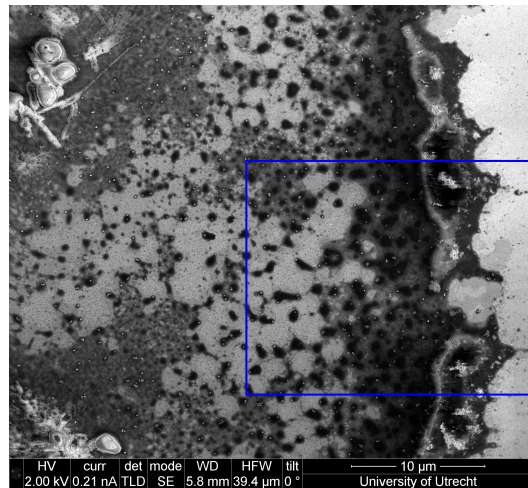
(b) Zoomed in on edge.
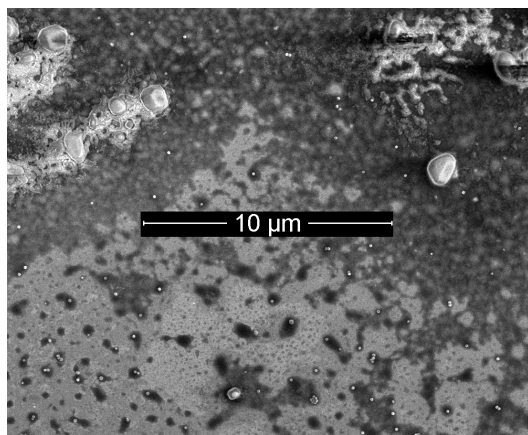
(c) Cropped part of (a).

(d) Cropped part of (b).

Figure 3.3: Zoomed in on framed parts of Fig. (3.2b).

3.2 Laser Ablation

The dropcasted samples are also imaged with the microscope from the ablation setup. As the size of the gold nano-particles is below the diffraction limit of the setup, we need additional SEM data to distinguish single particles from clusters of particles. Once particles are identified as single gold nano-particles we can perform measurements on them and perform data analysis.
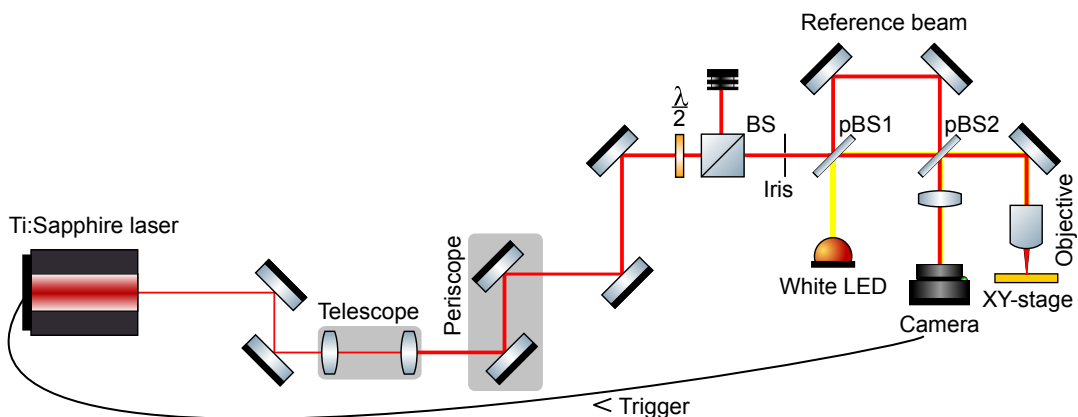
3.2.1 Setup

Figure 3.4: Overview of the ablation setup.

An overview of the ablation setup is given in Fig. (3.4). The TI:Sapphire laser (Mira 900, Coherent Inc.) provides 800 nm pulses with a duration of 150 fs and a repetition rate of 54 MHz. Attached to the laser is a Pulse Switch (Coherent Inc.) which is used to select pulses. The laser beam first passes the telescope which consists of a 50 mm and 125 mm lens, 211 mm apart, which expands the beam by a factor of 2.5. The lenses are a bit further apart than the sum of their focal lengths. This is done to compensate for the slightly divergent beam emitted by the laser and to obtain a weak focus on the back focal plane of the microscope objective that is described below.

After the telescope, the beam gets raised to the height of the microscope by a periscope and then passes an energy control system that combines a $\lambda/2$ wave plate and a beam splitter cube (BS). The wave plate is mounted on a motor controlled rotational stage (T-RS60A, Zaber Technologies Inc.) which enables precise control of the polarization and thus the amount of light transmitted by the beam splitter. This way a contrast ratio of 3000 is achieved. [8]

An iris is placed behind the first beam splitter to make the beam circular. This is essential in order to obtain an undistorted beam profile at the sample.
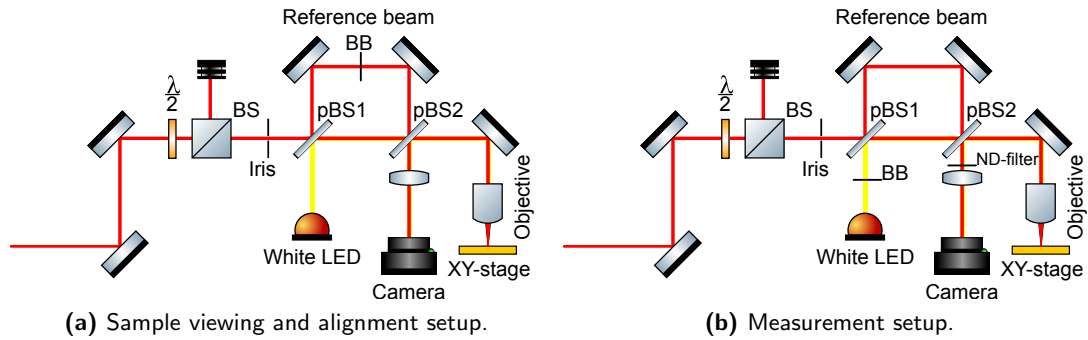
(a) Sample viewing and alignment setup.   **(b)** Measurement setup.

Figure 3.5: A section of Fig. (3.4) with added beam blocks (BB) and ND-filter for different applications.

The beam then passes a pellicle beam splitter (Thorlabs BP108, pBS1 in the figure). Its transmission and reflection are 93.9% and 6.1% respectively, for 800 nm light (specified by the manufacturer). The reflected beam is the reference beam in the figure. Both beams pass another pellicle beam splitter (Thorlabs BP145B2, pBS2 in the figure) with a specified transmission and reflection of 65.2% and 34.8%, respectively. The reference beam is transmitted to the camera and the main beam gets transmitted towards the sample. The main beam is then directed down into an NA=0.8 objective and focussed on the sample. The objective is mounted on a motor controlled translation stage (T-LSM025A, Zaber Technologies Inc.), which allows the objective to move in the z-direction with a 48 nm resolution.

Next, the light is focussed onto the sample by the objective to a spotsize of approximately 700 nm ($1/\text{e}^2$ radius). The sample is placed on a motor controlled xy translation stage (M-686.D64, Physik Instumente). Finally, the light scattered and reflected by the sample travels back through the objective and gets reflected into the camera (Andor Zyla 5.5) by the second pellicle beam splitter (pBS2).

3.2.2 Method

This section will provide an overview of the ablation and data acquisition method. A part of a dropcasted droplet viewed under LED illumination (Fig. (3.5a)) is shown in Fig. (3.6a). The bright white spots are gold particles and the dark spots are specs of dust. A SEM image of the blue part in the figure is pictured in Fig. (3.6b). We can now map the two images together, using the specs of dust as markers. The specs of dust are indicated by white numbers in the figures. Zoomed in versions of the optical and SEM images are given in Figs. (3.6c and 3.6d) respectively. When comparing the two images, it is immediately clear that the optical data alone is not enough to distinguish individual gold nano-particles, because what seem to be three particles in the optical image, are actually five particles in the SEM image.
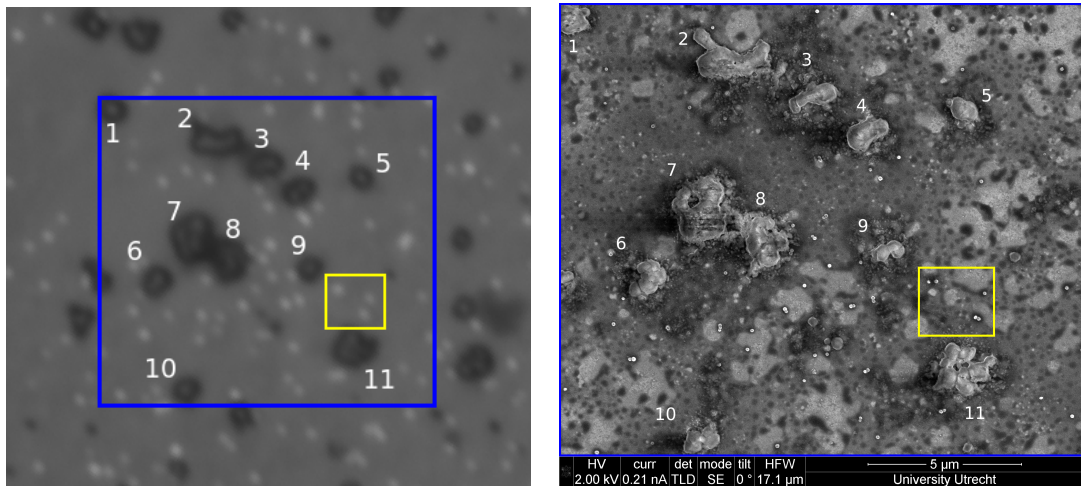
(a) Optical image of a dropcasted droplet under LED illumination.

(b) SEM image of the blue enclosed rectangle of (a).
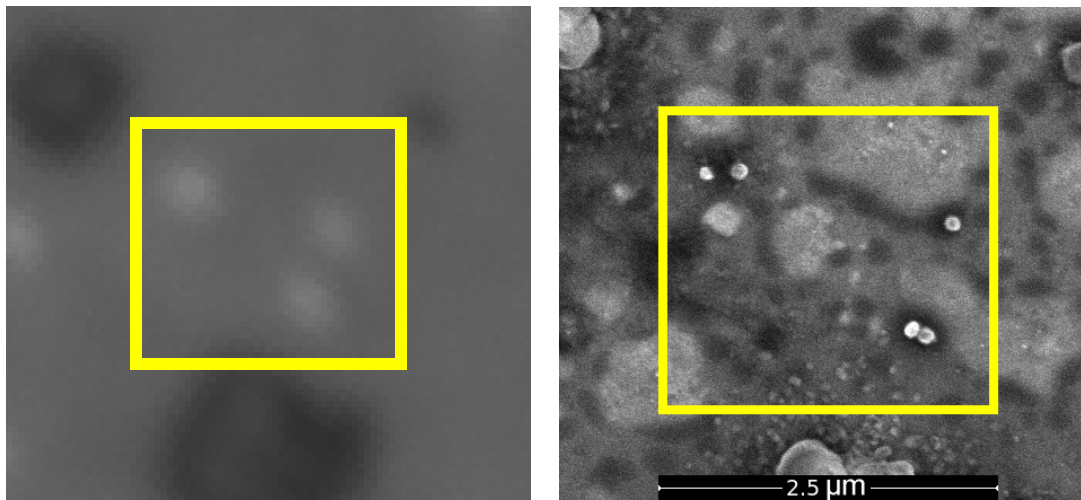
(c) Zoom in on optical image seems to reveal three gold nano-particles.

(d) Zoom in on SEM image reveals five gold nano-particles.

Figure 3.6: Mapping strategy. Blue and yellow rectangles hold the same surface respectively. The white numbers identify the same dust particles in different imaging methods.

Using the mapping procedure described above we can select a single gold nano-particle to ablate. To be within 4% accuracy of the fluence received by the particle, we need to align it within $100\,\mathrm{nm}$ of the center of the beam (assuming a $700\,\mathrm{nm}$, $1/e^2$ radius).

For the alignment method the reference beam is blocked and the white light LED is used to view the sample together with the beam, which is attenuated far below ablation threshold. This setup is depicted in Fig. (3.5a). A typical image of a particle with and without laser beam is shown in Fig. (3.7), where we look at the maximum of the scattered light.

The beam waist is about $700\,\mathrm{nm}$, the particles are $100\,\mathrm{nm}$ in diameter and the xy translation stage has a minimal incremental motion of $300\,\mathrm{nm}$. Alignment with this stage is very hard, because the incremental motion is three times bigger than a gold nano-particle. We, however, achieved alignment of the particles within $100\,\mathrm{nm}$ of the center of the spot by using the error in the bidirectional repeatability.

We start aligning by focusing the attenuated laser with the z-stage mounted objective on the ITO substrate near a selected gold nano-particle. Then the xy stage is moved such that the particle enters the beam and we see an increase in scattered laser light. The next goal is to maximize this scattering by centering the particle into the beam. This is done by moving the stage back and forth, where we use the error in the bidirectional repeatability to our advantage. First, the particle is aligned in the x-direction and then the y-direction.

Once the particle is aligned, a few beam blocks and ND-filters need to be swapped prior to measuring. The measurement setup is depicted in Fig. (3.5b), where the LED is blocked, the reference beam is unblocked and an ND-filter is placed in front of the camera to prevent it from saturation.

Laser triggering is based on an AND gate which provides a signal to the Pulse Switch when the camera is ready to capture data and a button is pressed when we want to measure. The Pulse Switch constantly leaks pulses with an intensity of about $1/50000$ with respect to its main output [8]. To minimize the effect of this leakage during measurements, the camera shutter time is set to its lowest value of $50\,\mathrm{\mu s}$. When the laser has fired its pulse, the reference beam and the scattered beam end up on different locations on the camera's active area for analysis.

The beam does not only illuminate the gold nano-particle, but also the ITO substrate. Therefore, also background measurements need to be performed in order to quantify the effect of scattering due to the substrate.
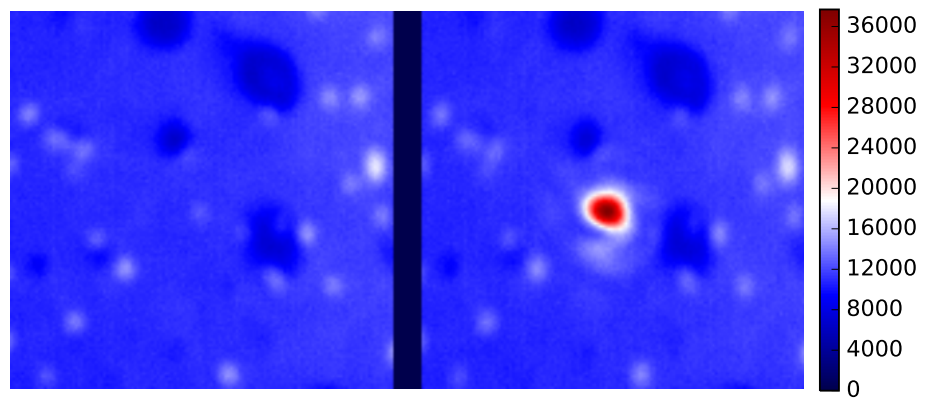
Figure 3.7: False colour camera image of gold nano-particles. Left: laser off. Right: laser on. A gold particle centered in the focussed laser beam shows in this case a maximum pixel value of about 36000.
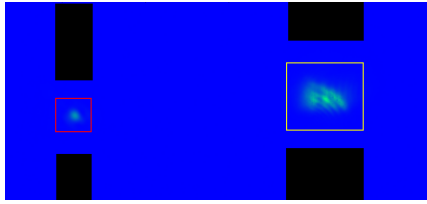
Figure 3.8: Spot scattered by sample (left) and reference spot (right) on camera image. The analysis algorithm first tries to find the reference spot and the sample spot. Afterwards, it sums ADU within a certain area around a spot to obtain a total ADU per spot. It then estimates the background per spot (black areas) and subtracts that from the total ADU count.

3.2.3 Data Analysis

The camera provides 16 bit greyscale images with information from the scattered beam and the reference beam, shown in Fig. (3.8) in false colours. For analysis we first look for the most intense spot which always corresponds to the reference beam. The second spot originates from the sample. Within a predefined area at the spot locations the *analog to digital units* (ADUs) are summed to obtain the total ADU per spot. Finally, the background contribution is estimated by averaging the background around the two spots separately and this average is subtracted from the total ADU.

Once the spots have been found and processed, the reflection or self-scattering of the particle during a measurement is calculated. This is done by dividing the sample spot total ADU by the reference spot total ADU.

3.2.4 Calibration

The ADU from the data analysis need to be converted to fluences to facilitate further analysis. To achieve this we placed a power meter directly under the objective, set at a distance enough not to be damaged, and put appropriate ND-filters in front of the camera to attenuate the reference beam intensity. This situation is illustrated in Fig. (3.5b).

A calibration measurement consists of recording the reading of the power meter, followed by a frame capture from the camera and another power reading. Since the power meter is optimized to measure CW beams, the laser is set to a repetition rate of $54\,\mathrm{kHz}$ to obtain a quasi-CW beam. The exposure time of the camera is set to $1\,\mathrm{ms}$ so it will integrate over 54 pulses during a measurement.

The calibration measurement is split up into three power regimes, which require three different ND-filters in front of the camera to prevent saturation. Tab. (3.1) gives an overview of the filters with their reported transmission percentages and the approximate power regimes as read from the power meter with their corresponding
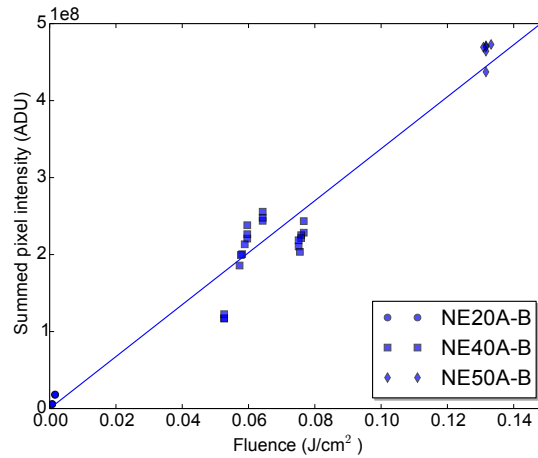
Figure 3.9: Calibration data. The slope of the fitted straight line gives the total ADU count to fluence conversion factor: $3.375 \pm 0.070 \times 10^9 \, \mathrm{ADU/(J/cm^2)}$, assuming a circular beam with a waist of $550 \, \mathrm{nm}$.

fluences. From the reading of the power meter we can calculate the energy per pulse: $E_{\mathrm{pulse}} = P/n$, with P the power read from the power meter and n the number of pulses per second. From this the fluence found for $1/e^2$ distance for a circular spot is calculated as follows:

$$F = \frac{2E}{\pi w_0^2} \, , \tag{3.1}$$

with w_0 the beam waist or the spot size at the sample, which is assumed to be $550 \, \mathrm{nm}$ for this calculation. In order for this calibration to work we need to compensate for different beam waists later on. Fig. (3.9) shows the measured calibration data. The ADU is corrected for each ND-filter with the transmission percentages provided in Tab. (3.1). Fitting a straight line to this data provides the total ADU to fluence conversion factor: $3.375 \pm 0.070 \times 10^9 \, \mathrm{ADU/(J/cm^2)}$.

Calibration	ND-Filter	T @ 800 nm (%)	Power regime (µW)	Fluence ($\mathrm{J\,cm^{-2}}$)
1	NE20A-B	5.6952	~ 0.20	$\sim 7.79 \times 10^{-4}$
2	NE40A-B	0.319979	~ 15.0	~ 0.06
3	NE50A-B	0.068068	~ 34.0	~ 0.13

Table 3.1: Calibration measurement setup parameters, with T the transmission of the ND-filter for the wavelength specified. The fluence is calculated using a beam waist of $550 \, \mathrm{nm}$.

3.3 Results and Discussion

The criterium for a successful measurement was the complete removal of the targeted particle in the optical image, which implies that the particle had to be close to the center of the beam. This requirement was not met for all measurements, which we attribute at least partly to vibrations in our setup due to construction and demolition work in the neighbouring building.
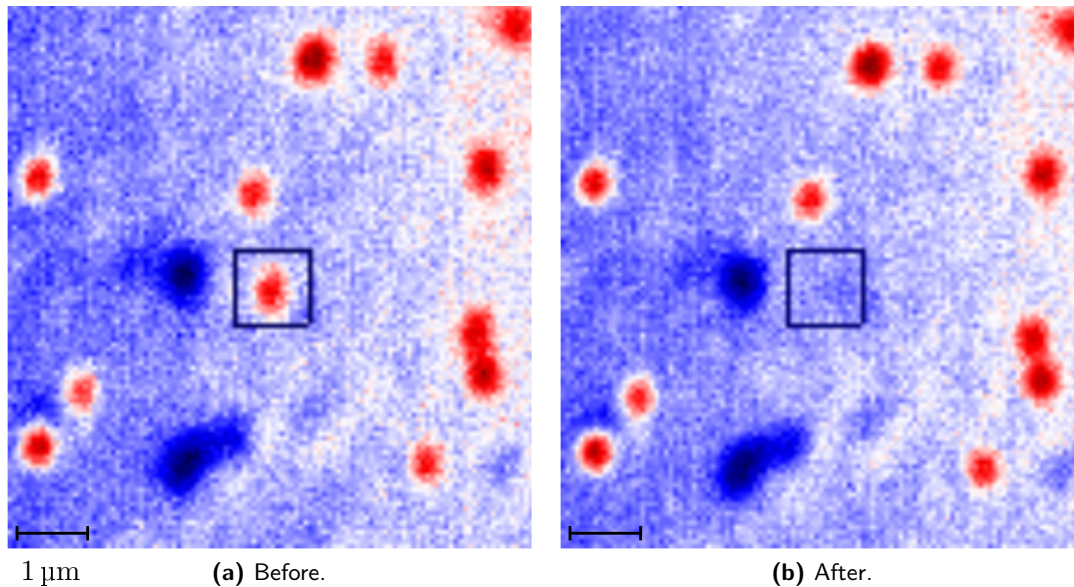

1 µm   **(a)** Before.   **(b)** After.

Figure 3.10: Typical before and after pictures from a successful single shot ablation measurement. The red dots are gold nano-particles.

A typical picture before and after the nano-particle ablation is displayed in Fig. (3.10), in which the blue square pictures the region of interest. Fig. (3.10b) clearly shows that the targeted particle is gone. Out of 69 targeted gold nano-particles, 52 were gone afterwards. The self-scattering as a function of fluence of these particles is shown in Fig. (3.11) as black disks with numbers to their top right, indicating the order in which they were taken. A series of measurements on gold nano-particles was always accompanied (mostly preceded) by a series of nearby ITO reference measurements. These are presented by open circles with letters and numbers combined and they provide data on the scattering of the substrate due to the incoming laser light. From the data in Fig. (3.11) we can not clearly see a difference between the scattering of gold nano-particles and ITO background measurements, which suggests that the gold nano-particles scatter the incoming laser light about the same as ITO. This is in contrast to our observations during alignment where we clearly saw an increase in scattered light when a particle came close to the center of the beam. We can put an upper limit on the ablation threshold by looking at what minimal fluence ablation
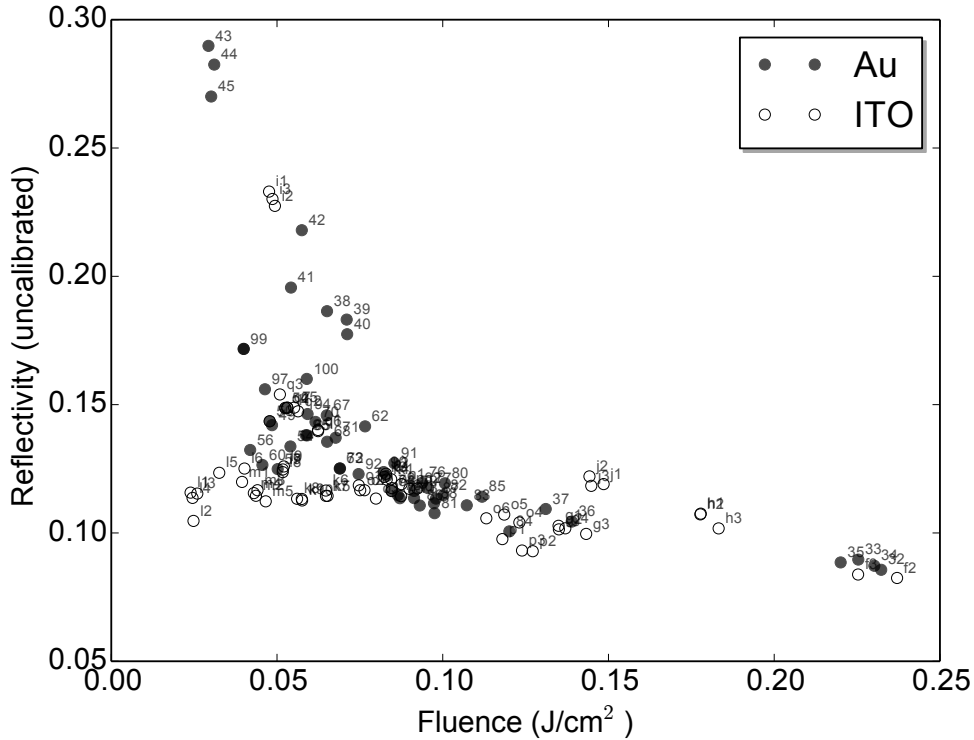
Figure 3.11: Self-scattering of ablated gold nano-particles (black disks) and ITO as reference (open circles). The numbers are different gold nano-particles and are used for reference later on. The letters with numbers in sequence (i.e. 'i1', 'i2' and 'i3') depict ITO reference data from the same location on the sample, taken in rapid succession. The fluence is calibrated using the calibration mentioned above with a constant and circular beam waist.

occurred. From Fig. (3.11) this value is about $0.03\,\mathrm{J\,cm^{-2}}$.

To get a better understanding of the data we went ahead by checking whether the previous assumption of a circular beam and constant beam waist was valid. We did this by fitting the ITO reference measurement data to a two-dimensional Gaussian centered around (x_0, y_0) and allowing a rotation of θ:

$$f(x,y) = A\mathrm{e}^{-2\left(\frac{B(x,y)}{\sigma_{\tilde{x}}^2} + \frac{C(x,y)}{\sigma_{\tilde{y}}^2}\right)} + D\,, \tag{3.2}$$

with

$$B(x,y) = (x - x_0)^2 \cos^2(\theta) + (y - y_0)^2 \sin^2(\theta) + (x - x_0)(y - y_0)\cos(\theta)\sin(\theta)$$
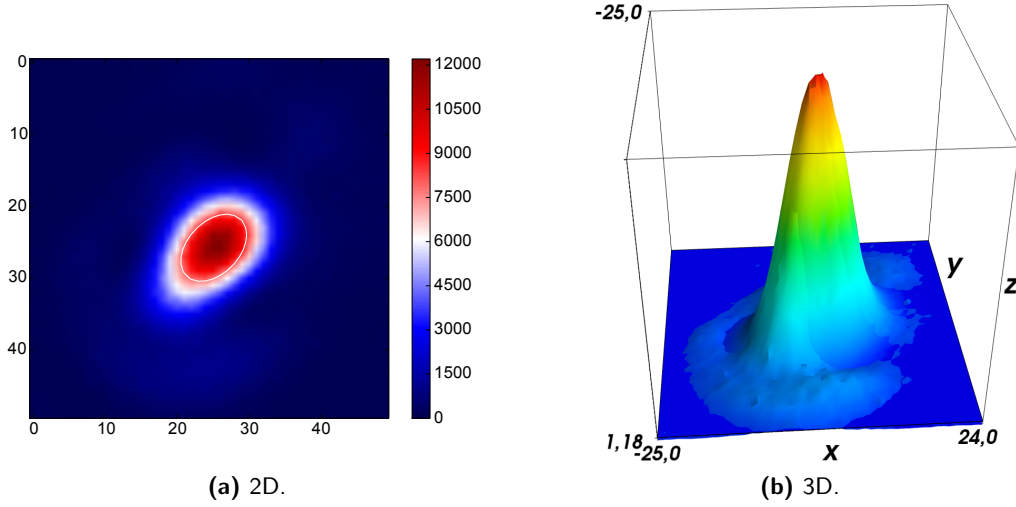
and

(a) 2D.　　　　　　　　　　　　**(b)** 3D.

Figure 3.12: Graphical representation of typical results of the fitting procedure. The white ellipse in (a) is a result of the fitting procedure and shows a large size difference between the semi-minor and semi-major axis. (b) shows the data together with the fit, with some minor deviations around the top.

$$C(x, y) = (x - x_0)^2 \sin^2(\theta) + (y - y_0)^2 \cos^2(\theta) - (x - x_0)(y - y_0) \cos(\theta) \sin(\theta) \,.$$

A graphical representation of a fit to ITO reference measurement 'i3' is shown in Fig. (3.12). From this fit we can extract the parameters σ_x and σ_y. These sigmas are the radii where the Gaussian intensity shows a $1/e^2$ decrease. The surface of the ellipse spanned by this Gaussian is $A_{\text{ellipse}} = \pi \sigma_x \sigma_y$. This quantity is plotted in Fig. (3.13) for each series of ITO reference measurements. The entries at $0\,\text{s}$ originate from data of the alignment procedure, which are due to leaked pulses (like Fig. (3.7), but on bare ITO without a gold nano-particle). Consecutive entries in the figure are from ITO reference measurements, which show large fluctuations in beam waist. These fluctuations arise from vibrations affecting the vertical position of the XY-stage or objective and will cause the beam to defocus and thus increase its waist.

Since the spot size fluctuates during ITO measurements, this behaviour must also be present during measurements on gold nano-particles. To check for fluctuations in spot size, the same fitting procedure has been applied to the gold measurements. The results are shown in Fig. (3.14) where fluctuations up to a factor of 2 in beam cross-section area arise (i.e. compare 33 to 72).

These fluctuations in spot size for ITO and gold mean that we have to compensate by multiplying the fluence as calculated in Eq. (3.1) by the following factor: $\frac{w_0^2}{\sigma_x \sigma_y}$, with $w_0 = 550\,\text{nm}$ and σ_x and σ_y result from the fitting procedure for each measurement. The entries in Fig. (3.11) have been corrected by this factor and are displayed in
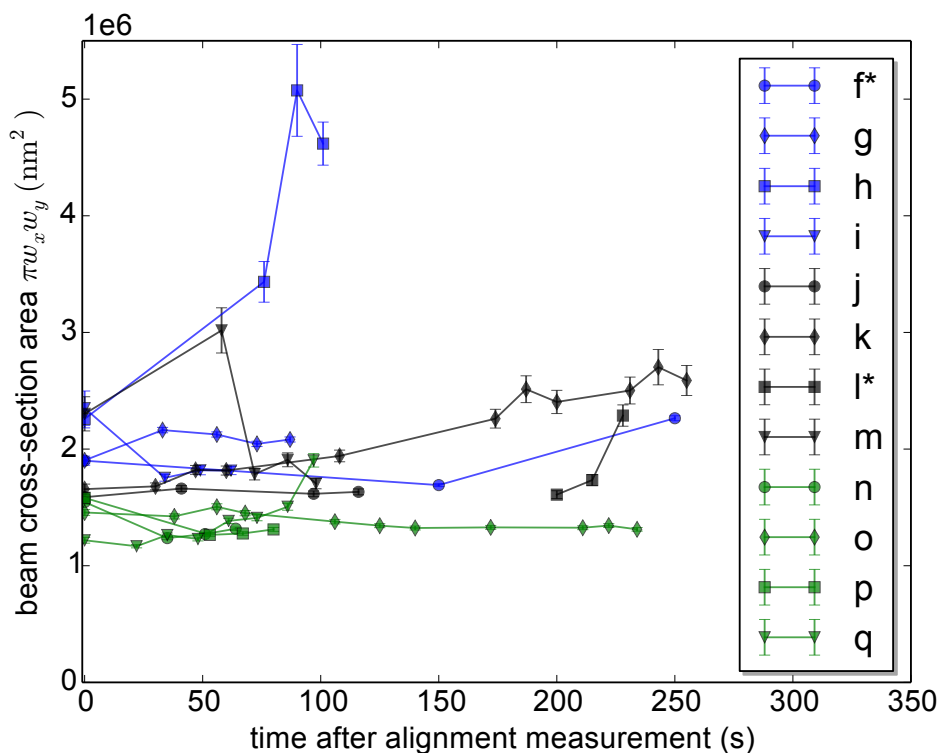
20

Figure 3.13: Beam cross-section fluctuations of ITO reference measurements. The entries at $0\,\mathrm{s}$ originate from the alignment procedure. Consecutive connected entries are from ITO reference measurements. The x-axis shows the amount of time after the aligment procedure and ideally all entries should follow one horizontal line, so there is no fluctuation in beam waist. The letters correspond to entries in Fig. (3.11). The initial time difference for reference f* is shortened to make it fit on this scale. Reference l* is missing initial alignment data.
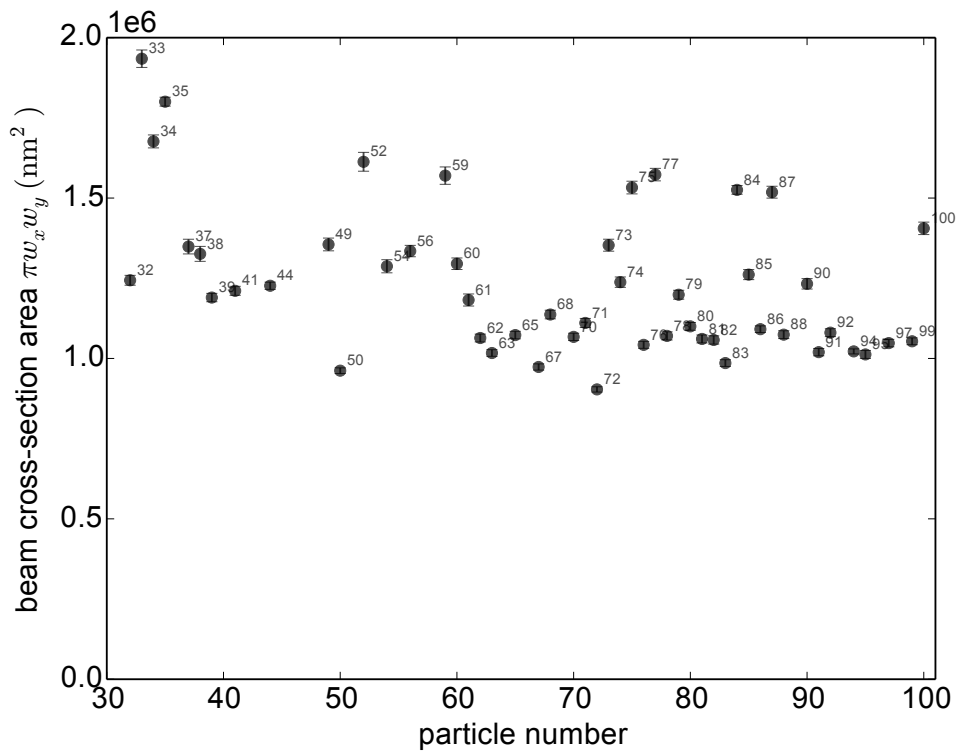
Figure 3.14: Beam cross-section fluctuations of measurements on gold nano-particles. The numbers correspond to entries in Fig. (3.11). Just like with the ITO reference measurements there ideally should be no fluctuation in beam waist.
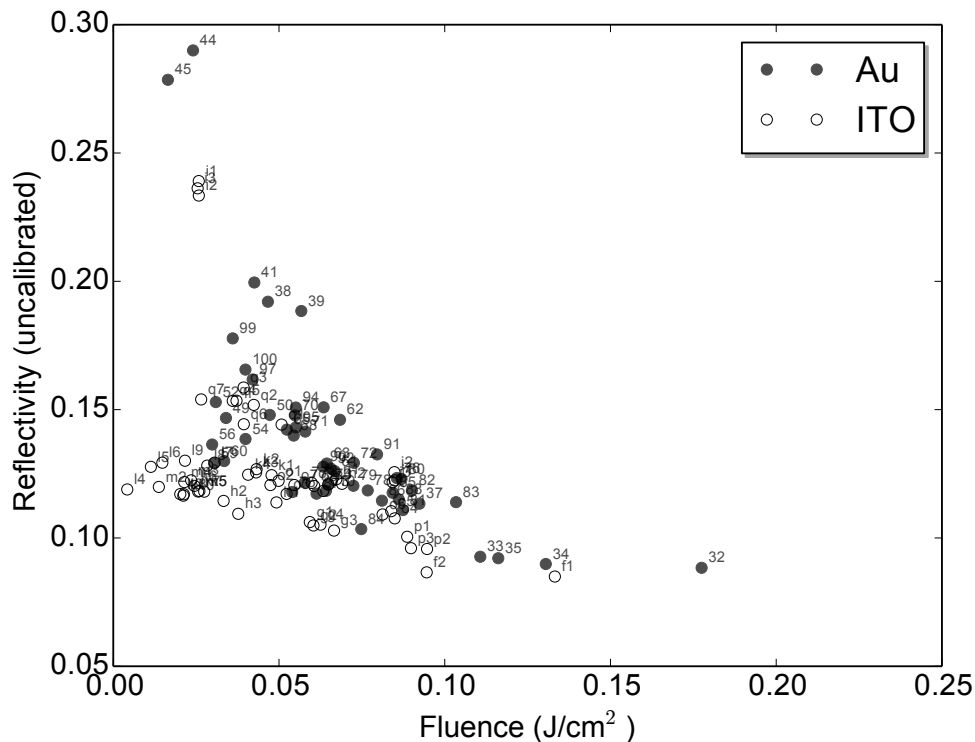
Figure 3.15: Spot size corrected version of Fig. (3.11). Self-scattering of successfully ablated gold nano-particles (black disks) and ITO as reference (open circles).

Fig. (3.15). A quick comparison between the two graphs indicates that all entries have been shifted to the left after the spot size correction has been applied. This is not unexpected, since the spot size was underestimated at first. The correction, however, does not yield a new insight in the behaviour of the self-reflectivity of the gold nano-particles when compared to the ITO reference measurements when we look at the graph as a whole. If we look at groups of entries, some noteworthy features can be spotted. Firstly, entries i1, i2, i3, 44 and 45 (top left) have a higher reflectivity than the others and they also happen to be measured close to each other in time (taken within 3 hours). Secondly, entries f1, f2, 32, 33, 34 and 34 (lower center) have a lower reflectivity than the others and they are also close to each other in time. Furthermore, the entries p1, p2, p3, 83, 84 (left above f2) and a few others are also close to each other in reflectivity and time. More entries can be grouped together like this and an overview of coupled measurements is presented in Tab. (3.2).

To find a general trend in gold nano-particle reflectivity with respect to the ITO background we divided the self-reflectivity of the gold nano-particles by the mean self-reflectivity of linked ITO reference measurements. This resulted in Fig. (3.16), where entries of the same colour and shape are linked to an ITO reference measurement

ITO	measurements	linked to gold nano-particle measurements
f	1, 2	32, 33, 34, 35
g	1, 2, 3, 4	37
h	1, 2, 3	38, 39, 41
i	1, 2, 3	44, 45
j	None	None
k	None	None
l	7, 8, 9	49, 50, 52, 54
m	2, 3, 4, 5	56, 59, 60
n	1, 2, 3	61, 62, 63, 65, 67, 68, 70, 71, 72
o	8, 9, 10	73, 74, 75, 76, 77, 78, 79, 80, 81, 82
p	1, 2, 3	83, 84, 85, 86, 87, 88, 90, 91, 92, 94, 95
q	1, 2, 3, 4, 5, 6, 7	97, 99, 100

Table 3.2: ITO (left) measurements linked to gold nano-particle measurements (right). The letters and numbers can be found in Fig. (3.11). 'f 1, 2' means that the entries 'f1' and 'f2' have been used. The linking is based on the measurements being close to each other in time (taken within 3 hours).

according to Tab. (3.2). A very important aspect of the graph is that the normalized self-reflectivity of most gold nano-particles lies above 1.0. This means that the gold particles scatter more of the laser pulse back into the objective than ITO. Over the course of the graph, the reflectivity also seems to go down, which is in accordance to [6] on bulk gold.

In conclusion, we have achieved ablation of gold nano-particles on ITO using a 150 fs laser pulse from a relatively low power laser source. But due to the high amount of ITO scattering we cannot say anything quantitative of the gold self-reflectivity. When normalizing the gold nano-particle reflectivity to ITO reference measurements we do see that the particles in general scatter more light that the substrate which is what we observed during aligning.

For further research, it would be advantageous to cancel the effect of scattering due to a substrate background. To achieve this, dark field imaging can be used [9]. The low power output of our laser did not allow for this. Another option would be to suspend the gold nano-particles in free space using a quadrupole magnetic trap ([10] and [11]).
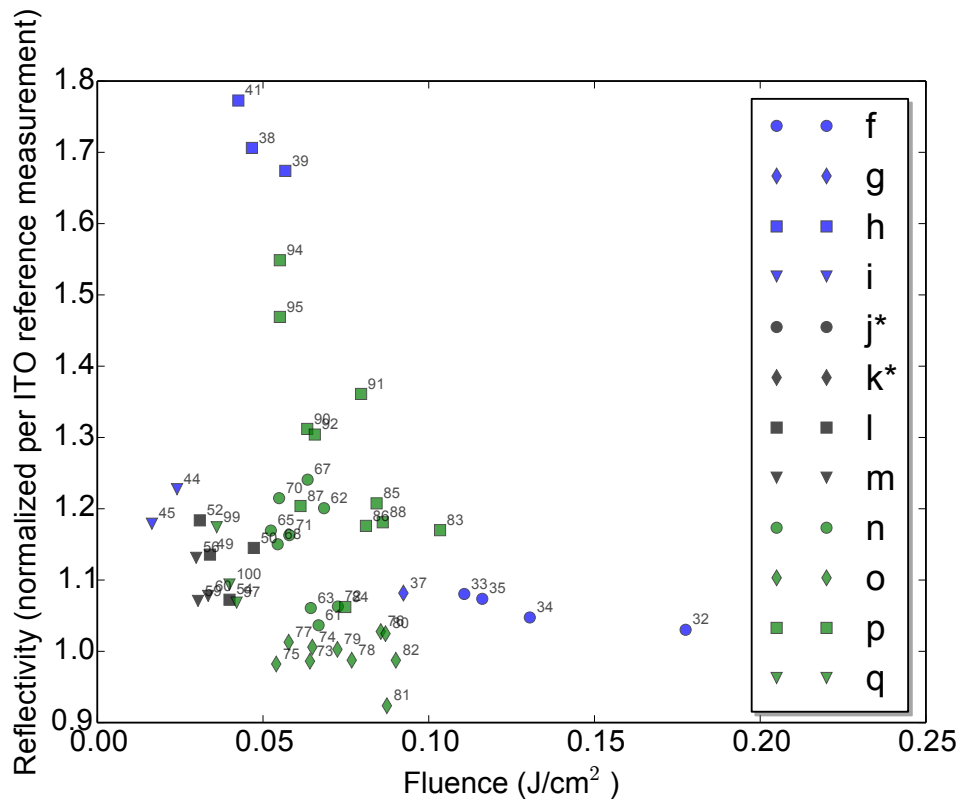
Figure 3.16: Normalized self-scattering from a selection of gold nano-particles of Fig. (3.11). The selection consists of the gold nano-particle entries in Tab. (3.2) from which the self-scattering is divided by the self-scattering of ITO reference measurements. There are no entries in this graph for ITO measurements j* and k*.

4 Simulations

In the previous chapter we described an experiment involving an interaction of femtosecond laser light with gold nano-particles. We investigated the reflectivity as a function of incident fluence. In this chapter we describe a simulation of a femtosecond laser pulse interacting with a gold nano-particle. We investigate the scattered energy as a function of fluence.

We will explain how the equations from Sec. (2) find their way into the model, aided with some visualizations in the form of block diagrams. We then continue by presenting intermediate results, followed by the end results with a discussion and conclusion.

4.1 Method

In our simulations we use a pulsed laser described by the following intensity

$$I(t) = I_{\text{peak}} e^{-\left(\frac{t}{t_{\text{pulse}}}\right)^2} , \tag{4.1}$$

with t_{pulse} the pulse duration and I_{peak} the peak intensity. The pulse duration is set to $100\,\text{fs}$, corresponding to a FWHM of about $160\,\text{fs}$. The peak intensity is given by

$$I_{\text{peak}} = \frac{\sqrt{\pi} F}{t_{\text{pulse}}} ,$$

with F the fluence, which ranges from 10^{-4} to $10\,\text{J}\,\text{cm}^{-2}$ in the simulation. The total time range in the simulation extends from -500 to $500\,\text{fs}$ with a time-step $\Delta t = 1\,\text{fs}$.

The simulation consists of two parts. First, the temperature of the electron gas $T_{\text{e}}(t)$ of the gold particle is calculated and saved for each time-step during the laser pulse. The second part uses this to calculate the energy that is scattered by the particle.

4.1.1 Heat Equation

To obtain $T_{\text{e}}(t)$, we have to integrate the heat equation Eq. (2.9)[1] over time. The heat equation consists of several components which are ordered below according to dependency

---

[1] The numerical integration is done by using the Python package 'scipy.integrate.odeint' which uses lsoda from the FORTRAN library odepack.

$$\underbrace{\frac{\partial[T_{\mathrm{e}}(t)]}{\partial t}}_{\text{depends on:}} = \underbrace{\frac{\sigma_{\mathrm{abs}}}{C_{\mathrm{e}}}}_{\text{temperature}} \quad \underbrace{I(t)}_{\text{time}} \quad \underbrace{\frac{1}{V}}_{\text{constant}} . \tag{4.2}$$

We will describe the integration of the components on the right hand side of the equation into the model. Firstly, the absorption cross-section σ_{abs} depends on the dielectric function, which depends on the damping time τ and the plasma oscillation frequency ω_{p}. The last two both depend on the total number of conduction electrons per atom Z_{eff}, which is a temperature dependent input parameter. The plasma oscillation frequency depends on the number of free electrons per atom N, so we apply the transformation

$$\omega_{\mathrm{p}}^2 = Z_{\mathrm{eff}}\omega_{\mathrm{p,0}}^2 , \tag{4.3}$$

where $\omega_{\mathrm{p,0}}$ is a value obtained from literature, listed in Table (4.1). As explained in Sec. 2.3, Fourment et al. experimentally determined Z_{eff} for a large temperature range. Their data is plotted in Fig. (4.1) and is fitted to a simple spline function

$$y(x) = \begin{cases} 1 & \text{if } y \leq 1 \\ y(x) & \text{if } y > 1 \end{cases} .$$

Secondly, the electron heat capacity C_{e} cannot be considered constant over the temperature range in our model. Z. Lin and L. V. Zhigilei [12] calculated the electron heat capacity for several metals based on their electron density of states. They did this for temperatures typically reached in femtosecond laser processing. Their data for gold is plotted in Fig. 4.2, together with an interpolation function. As a comparison, the heat capacity of a classic free electron gas $\frac{3}{2}Nk_{\mathrm{B}}$ and the heat capacity using quantum theory $\frac{\pi^2}{2}Nk_{\mathrm{B}}\left(\frac{T}{T_{\mathrm{F}}}\right)$ [13] are also plotted. The values of N, k_{B} and T_{F} are listed in Table (4.1). For temperatures up to $2000\,\mathrm{K}$, the quantum model excellently agrees with the data from Lin and Zhigilei, which is expected because the quantum model should be valid for $T \ll T_{\mathrm{F}}$.

Thirdly, the pulse intensity $I(t)$ is an input parameter given by eq. (4.1). Finally, the volume $V = \frac{4}{3}\pi a^3$, with a the radius of the particle, is constant throughout the simulation.

The equations and input parameters that are part of the heat equation are depicted in Fig. (4.3).
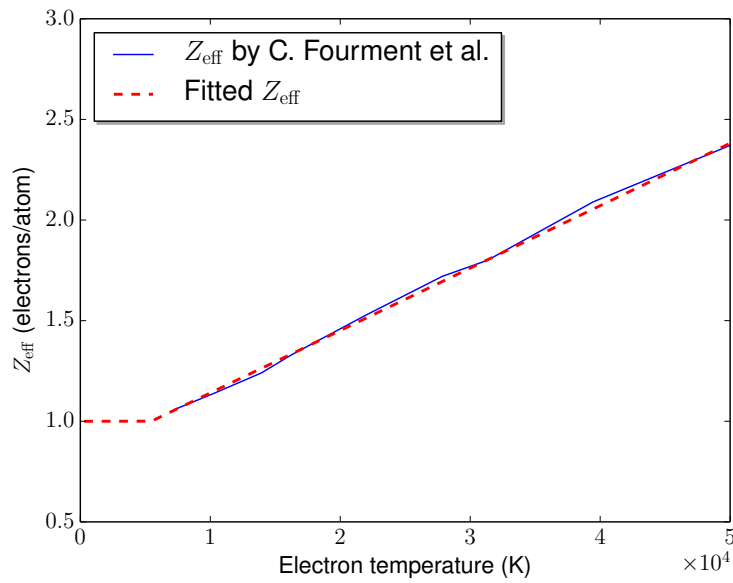
Figure 4.1: Effective number of conduction electrons per atom against electron temperature. Data is obtained from [5].
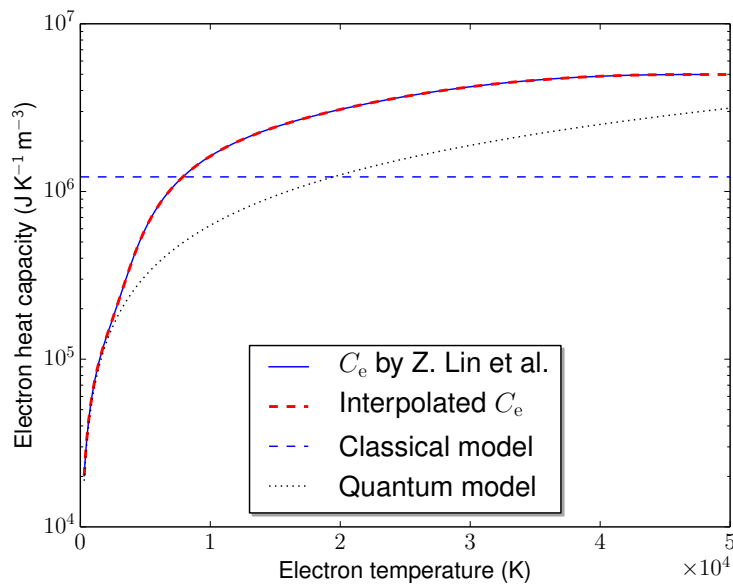

Figure 4.2: Electron heat capacity C_e obtained from [12] (solid blue) plotted against electron temperature. The classical picture $\frac{3}{2}Nk_\mathrm{B}$ and the quantum picture $\frac{\pi^2}{2}Nk_\mathrm{B}\left(\frac{T}{T_\mathrm{F}}\right)$ are also plotted as comparison.
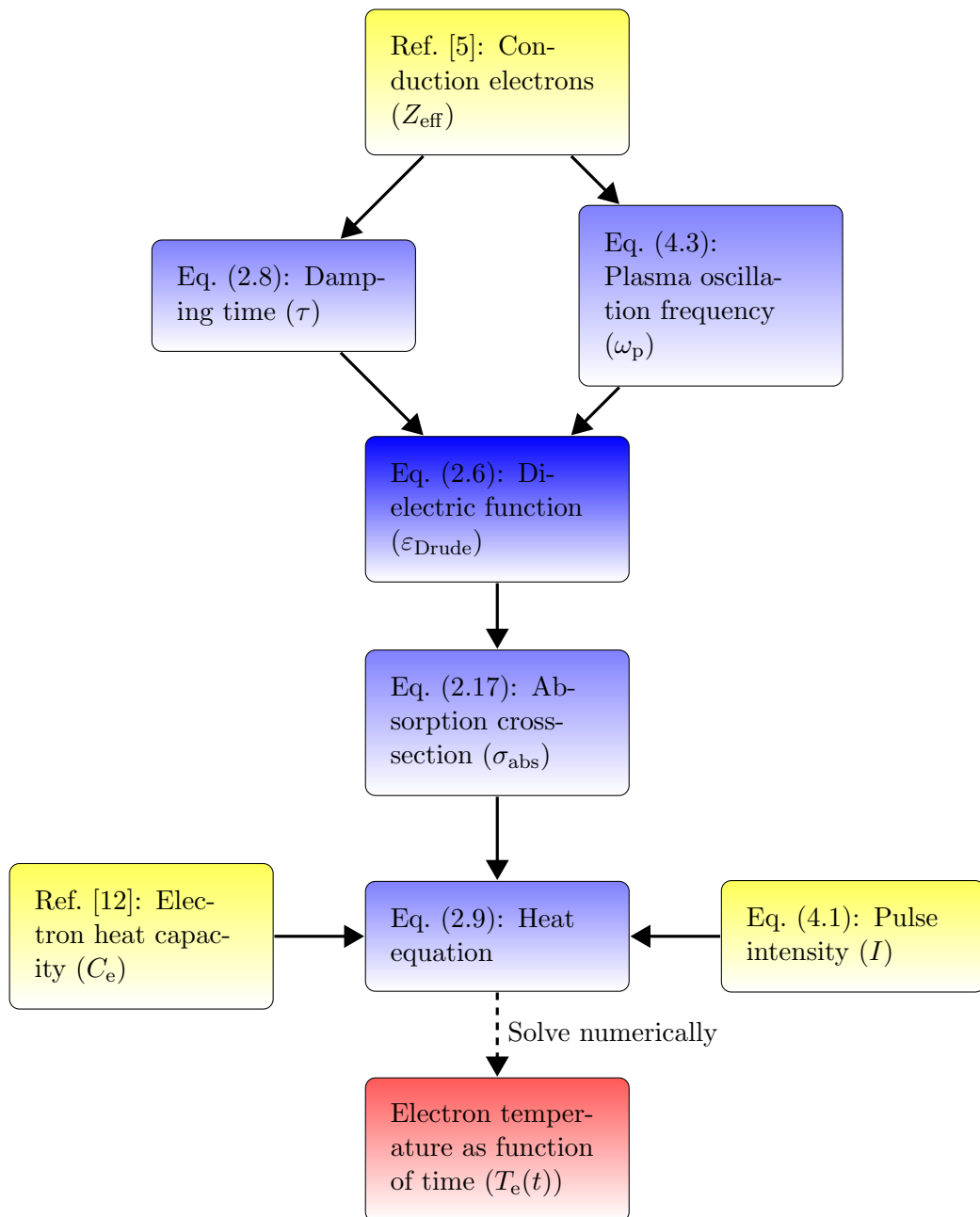
Figure 4.3: Graphical representation of the required equations (blue) and input parameters (yellow) that lead to solving the heat equation.

4.1.2 Scattered Energy

The flow chart in Fig. (4.5) shows a graphical representation to obtain the scattered energy. The steps that lead to the dielectric function are similar to Fig. (4.3), with the exception that the electron temperature T_e is used to calculate the number of free conduction electrons for each time-step. This again leads to the dielectric function through the damping time and the plasma oscillation frequency. Through Eq. (2.16) the scattering cross-section is obtained from the dielectric function.

The scattered power is obtained by simply multiplying the scattering cross-section with the pulse intensity

$$P_{\text{scat}}(t) = \sigma_{\text{scat}}(t)I(t) \,. \tag{4.4}$$

We then get the total scattered energy by integrating the scattered power over time

$$E_{\text{scat}} = \int P_{\text{scat}}(t)\mathrm{d}t \,.$$

The discritized version of the scattered energy is

$$E_{\text{scat}} = \Delta t \sum_t P_{\text{scat}}(t) \,. \tag{4.5}$$

Only a fraction of the electric field scattered by the particle enters the objective as sketched in Fig. (4.4. If we approximate the scattered or emitted electric field due to a dipole as radially symmetric near the objective, we can define the scattering ratio R_{scat} as the surface of the sphere that fits the objective divided by the total surface of the sphere. Geometry gives

$$R_{\text{scat}} = \frac{S_{\text{cap}}}{S_{\text{sphere}}} = \frac{2\pi r^2(1 - \cos\theta)}{4\pi r^2} = \frac{1}{2}(1 - \cos\theta) \,,$$

where θ is the angle from the beam axis. For an NA = 0.8 objective the angle $\theta \simeq 53°$ and $R_{\text{scat}} \simeq 0.20$. We can obtain a reflectivity in terms of an effective scattering cross-section by dividing the total scattered energy by the incoming fluence

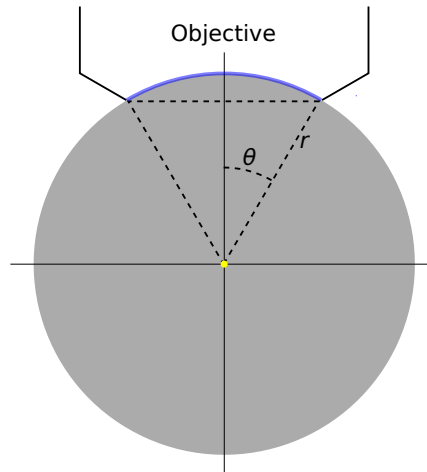$$\sigma_{\text{scat,eff}} = \frac{R_{\text{scat}}E_{\text{scat}}}{F} \,.$$

Figure 4.4: In blue is the part of the electrical field that enters the objective, originating from the particle at the center.

4.1.3 Variables and Parameters

The equations that govern the simulation contain a number of constants that are listed in Table (4.1) below.

symbol	description	used in Eq.	value
a	particle size (radius)	(2.15)	$50\,\mathrm{nm}$
ε_0	vacuum permittivity	(2.15)	$8.854 \times 10^{-12}\,\mathrm{F\,m^{-1}}$
ε_1	dielectric function inside particle	(2.15)	$\varepsilon_{\mathrm{Drude}}$ Eq. (2.6)
ε_2	dielectric constant outside particle	(2.15)	1.0 (air)
ε_∞	offset to dielectric function	(2.6)	6.0
ω	light oscillation frequency	(2.6)	$2.355 \times 10^{15}\,\mathrm{Hz}$
$\omega_{\mathrm{p,0}}$	plasma oscillation frequency	(2.6)	$1.360 \times 10^{16}\,\mathrm{Hz}$
N	free electrons density for gold		$5.9 \times 10^{28}\,\mathrm{m^{-3}}$
k_{B}	Boltzmann constant		$1.38 \times 10^{-23}\,\mathrm{J\,K^{-1}}$
T_{F}	Fermi temperature for gold		$64\,000\,\mathrm{K}$

Table 4.1: Used constants. ε_1 is also listed here, but it is not constant in our simulations. The values of N, k_{B} and T_{F} are used in plots in some of the figures.

4.2 Results and Discussion

In this section we will present results from the simulation. We start by presenting some intermediate results before proceeding to the effective scattering cross-section.

The first interesting intermediate result is the behaviour of the electron temperature over time. This is plotted in Fig. (4.6), indicated by the solid curves, for several
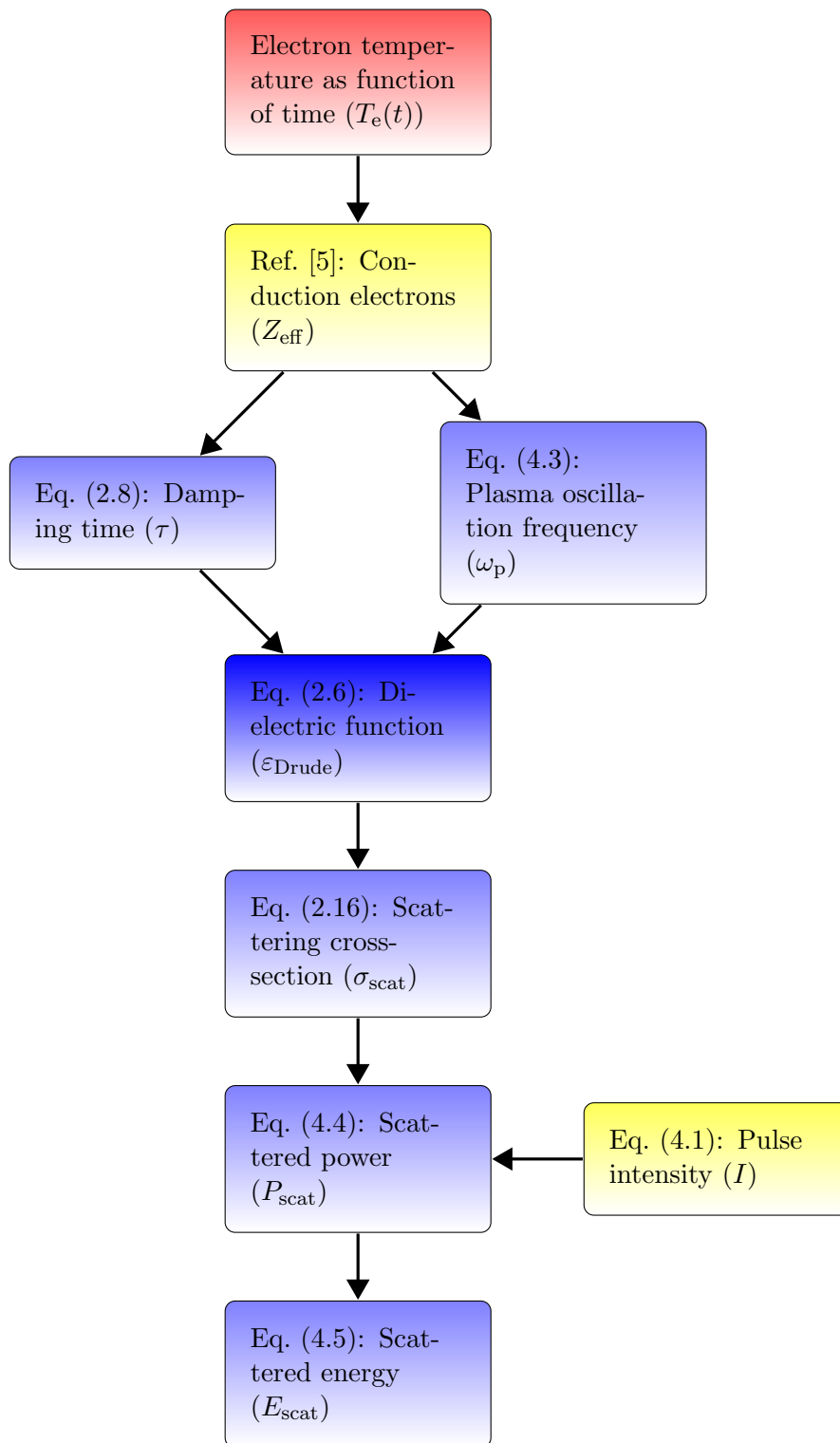
31

Figure 4.5: Graphical representation of the required equations (blue) and input parameters (yellow) that lead to the scattered energy.

fluences. The electron temperature curves clearly follow cumulative distributions, which start at 300 K and begin to rise when the pulse intensity, indicated by dotted curves, becomes significant.

The dashed line marked by $T_{e,max}|_{Z_{eff}=1}$ indicates the temperature at which the effective number of conduction electrons per atom becomes greater than 1, which happens at about 5500 K (see Fig. (4.1)). All temperature curves that go beyond this dashed line, show a change in slope slightly above it, caused by an increase in the density of conduction electrons.

Shown in the inset of the figure is the relation between the final electron temperatures and the maximum pulse intensities. We again observe a change in slope at around 6000 K and we see a slight decline in growth of the final electron temperature at higher pulse intensities. This decline is the result of the high electron heat capacity at these temperatures.

The electron damping time τ, given in Fig. (4.7), is very sensitive to the number of free conduction electrons. When Z_{eff} becomes greater than 5400 K, the damping time goes down very rapidly.

The maximum electron temperature $T_{e,max}$ reached in our model is 46 000 K for a fluence of $10.00\,\mathrm{J\,cm^{-2}}$. This maximum temperature is well within the limits of the experimental data of Z_{eff} by Fourment et al. and the calculated data of C_e by Lin and Zhigilei.

We now know the behaviour of the electron temperature under influence of the laser pulse and continue with results on the effective scattering cross-section. This cross-section is plotted in Fig. (4.8) together with the final electron temperature for fluences up to $1.5\,\mathrm{J\,cm^{-2}}$. For higher fluences, the final electron temperature goes up, which was evident from Fig. (4.6). The effective scattering cross-section starts to decrease at a fluence of about $0.8\,\mathrm{J\,cm^{-2}}$. At this fluence the electron temperature becomes high enough to generate extra conduction electrons. Note that our experiments did not reach fluences above $0.20\,\mathrm{J\,cm^{-2}}$, so we would not expect to see a change in reflectivity in this fluence range with respect to this model.

The model allows to go higher up in fluence, before the electron temperature becomes higher than the included experimental and calculated data. Fig. (4.9) shows the effective scattering cross-section and final electron temperature for fluences up to $10\,\mathrm{J\,cm^{-2}}$. Over the whole fluence range there is a drop in effective scattering cross-section of about 10 % while the electron temperature reaches 46 000 K.

In conclusion, we have modeled a gold particle with a diameter of 100 nm under influence of a laser pulse with a duration of 160 fs (FWHM). We have included experimental data from Fourment et al. on the number of free conduction electrons per atom with respect to temperature. We have also included data calculated by Lin and Zhigilei on the electron heat capacity with respect to temperature. For fluences up to
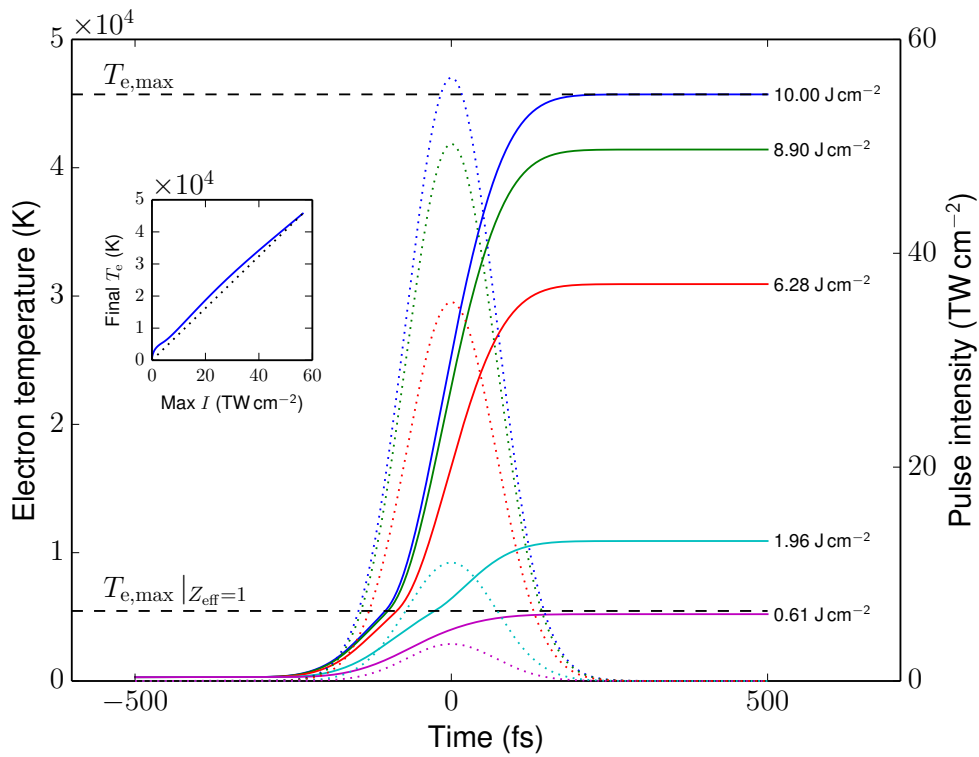
Figure 4.6: Electron temperature (solid) and pulse intensity (dotted) against time for six different fluences. The temperature at which the number of conduction electrons becomes greater than 1 is marked by $T_{\mathrm{e,max}}|_{Z_{\mathrm{eff}}=1}$ and is about $5500\,\mathrm{K}$. The maximum electron temperature $T_{\mathrm{e,max}}$ reached in the model is about $46\,000\,\mathrm{K}$. The solid blue curve in the inset shows the relation between the final electron temperature and pulse intensity. The straight black dotted line is a guide to the eye.
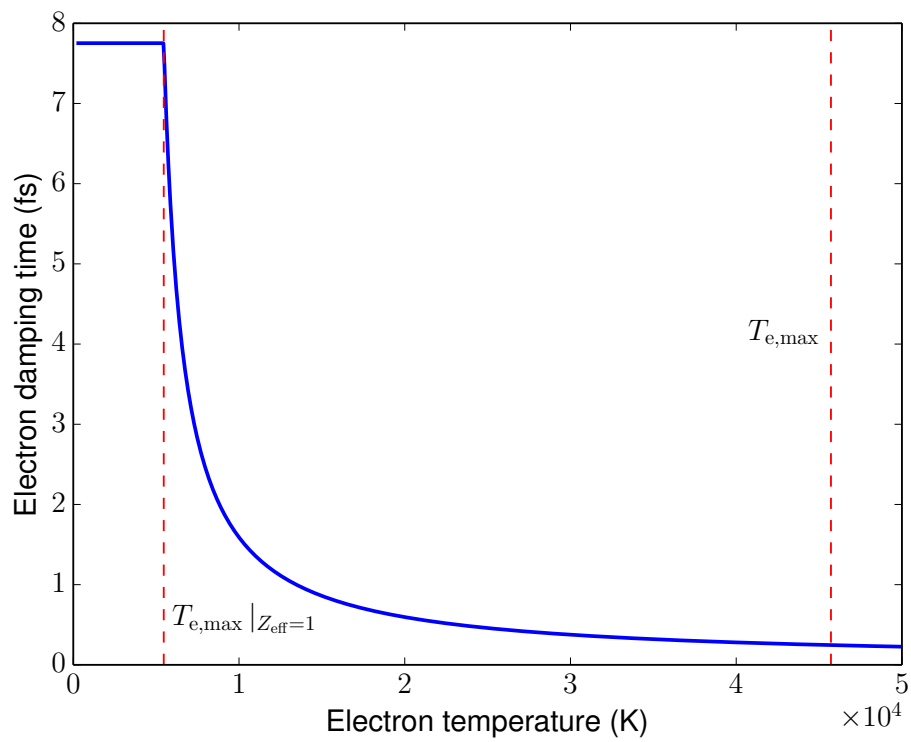
Figure 4.7: Electron damping time τ plotted against electron temperature. The steep drop occurs at the red dashed line marked by $T_{\mathrm{e,max}}|_{Z_{\mathrm{eff}}=1}$.

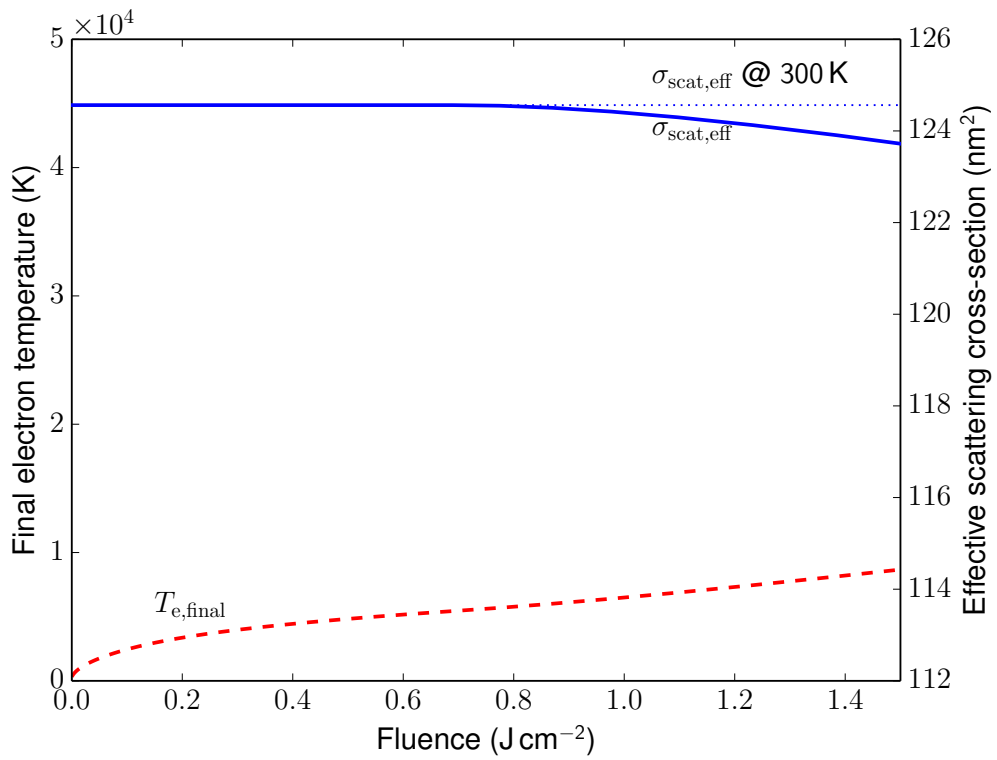**Figure 4.8:** Effective scattering cross-section (solid blue line) and final electron temperature (dashed red line) for fluences up to $1.5\,\mathrm{J\,cm^{-2}}$.

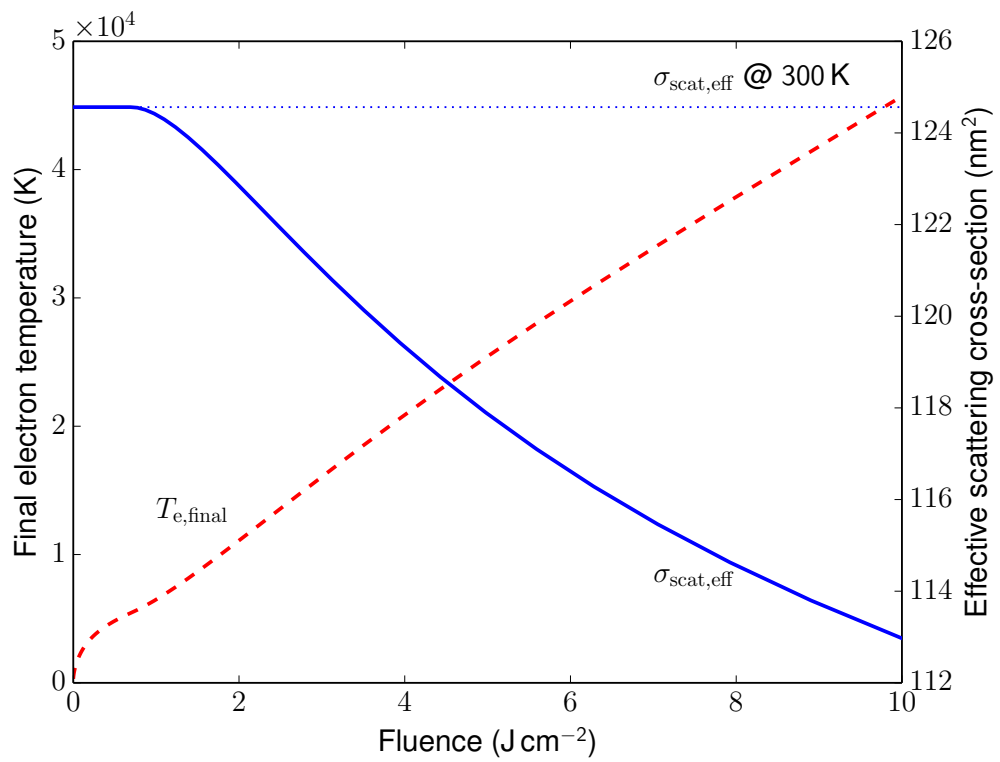**Figure 4.9:** Effective scattering cross-section (solid blue line) and final electron temperature (dashed red line) for fluences up to $10.0\,\mathrm{J\,cm^{-2}}$.

$10.0\,\mathrm{J\,cm^{-2}}$ the electron temperature in the model did not exceed the included data temperature range. The electron damping time in our model is very sensitive to the number of free conduction electrons; it goes down rapidly when Z_{eff} becomes greater than 1 at an electron temperature of $5400\,\mathrm{K}$. The reflectivity in terms of the effective scattering cross-section starts dropping at a fluence of about $0.8\,\mathrm{J\,cm^{-2}}$, when the electron temperature reaches $5400\,\mathrm{K}$. In total, the effective scattering cross-section goes down about $10\,\%$.

When comparing the effective scattering cross-section from our model with the self-reflectivity of a gold particle on glass coated with an ITO substrate from our experiments, we notice that the model predicts that there should be no change in reflectivity for fluences under $0.8\,\mathrm{J\,cm^{-2}}$. We should thus attribute the features that we see in the self-reflectivity to the ITO substrate in which case further research could investigate the simulation of a gold particle on such a substrate. An experimental approach would be to remove the ITO substrate in the experiments altogether.

As an outlook, further experiments, reaching fluences up to $10\,\mathrm{J\,cm^{-2}}$, should be conducted to check the results of our simulations and to check if our assumption of Rayleigh sized particles holds.

5   Conclusion and Outlook

In this thesis, the interaction between a femtosecond pulsed laser and gold nano-particles is investigated, both experimentally and with a simple model. We draw the following conclusions:

- We have successfully isolated single gold nano-particles from a solution and combined optical images with SEM data to allow us to distinguish single gold nano-particles during the ablation experiments.

- Femtosecond laser ablation of single gold nano-particles is achieved using a relatively low power laser. Their reflectivity as a function of fluence seems to be higher than the ITO substrate, but due to the high amount of ITO scattering we can not say anything about the reflectivity of the gold nano-particles themselves.

- Using a simple model, we have found that the reflectivity of gold nano-particles decreases above a fluence of $0.8 \, \mathrm{J \, cm^{-2}}$ and is decreased by $10\,\%$ at $10 \, \mathrm{J \, cm^{-2}}$.

The reflectivity results from the experimental part where governed by the ITO scattering. As an outlook we thus propose gold nano-particle ablation without a reflective substrate. Another option would be to use dark field imaging with a much more powerful laser than we used. This technique would cancel the scattering due to a substrate. Furthermore, the simulations provided interesting results, although they have yet to be verified by experiments in the fluence range of 1 - $10 \, \mathrm{J \, cm^{-2}}$.

6 Acknowledgements

When I started to work on this thesis in the Nanophotonics group I spent most of the time working together with Robbert Schoo on a project to include a digital micromirror device for beamshaping into the ablation setup. We collaborated on this for about half a year but then our projects took different directions. Our interest in both projects remained and I want to thank him for always questioning results and helping me understand the physics of my project.

I also want to acknowledge the other master students working in the ablation lab, Kostas Voutyras, Anne de Beurs, James Findley de Regt, Marcel Scholten, Jasper Clarijs and Karindra Perrier. I want to thank James Findley de Regt for my initial understanding of optics systems, his ever inspiring quotes of the day and pub crawl organization skills. Next up is Marcel Scholten, who I want to thank for always being available to refresh concepts in physics and help me understand problems we faced while working on the same ablation setup. I want to thank Jasper Clarijs for our discussions and views on the work we did. Finally, I want to thank Karindra Perrier for her jazz performances and ever cheerful presence.

The master students from the Bose Einstein condensation lab were never far and I would like to say a few words about them. First, I want to thank Qiao Li, who never failed to accompany me on coffee breaks where we discussed physics problems we faced, advances in ballroom dancing, other sporting activities and games. Next, I want to thank Koen Sponselee for always being there when I needed help on error propagation, better visualization of plotted data and the many epic games of ping pong.

I want to thank the PhD students Arjon van Lange, Sebastiaan Greveling, Sandy Pratama and Ole Mussmann for their feedback during group meetings and assistance in the lab. I especially want to thank Sebastiaan Greveling for our in-depth Python discussions and continuing my line of work on graphical user interface development. I also want to thank Sandy Pratama for his help on my initial Python coding problems and conveying his deep understanding of modeling optics systems. And of course I want to thank Ole Mussmann for his fantastic and enthusiastic presentations and discussions.

The technicians in our group deserve a lot of credit. I want to thank Dante Killian for making sure all the systems were in working order and for his entertaining remarks and discussions. I also want to thank Cees de Kok for making sure orders were placed and supplying us with clean optics. Lastly, I want to thank Paul Jurrius for a good working environment in the ablation lab, guiding me through my own little wood working projects, organizing borrels with bitterballen and beer pong, but mostly just having fun!

I want to thank my supervisor Dries van Oosten for supervising me and always being

there when I was stuck. I very much enjoyed his inspiring morning monologues on basically life, the universe and everything.

Finally, I want to thank the postdoc in our group, Javier Hernández who is going to continue this work and who supplied me with many useful suggestions and comments in the final phase of writing this thesis.

The Nanophotonics group as a whole deserves praise for the gezelligheid, warm atmosphere and team building events. I had a great time!

41

References

[1] B. C. Stuart, M. D. Feit, S. Herman, A. M. Rubenchik, B. W. Shore, and M. D. Perry, *Nanosecond-to-femtosecond laser-induced breakdown in dielectrics*, Phys. Rev. B **vol. 53**, pp. 1749–1761, URL http://link.aps.org/doi/10.1103/PhysRevB.53.1749 (1996) 1

[2] H. Zhang, *Single-shot femtosecond laser ablation on the nanoscale*, Ph.D. thesis, Utrecht University (2013) 1, 2.2

[3] B. Rethfeld, K. Sokolowski-Tinten, D. von der Linde, and S. Anisimov, *Timescales in the response of materials to femtosecond laser excitation*, Applied Physics A **vol. 79**, no. 4, pp. 767–769, URL http://dx.doi.org/10.1007/s00339-004-2805-9 (2004) 2.1

[4] L. Novotny and B. Hecht, *Principles of nano-optics* (2006) 2.2, 2.5

[5] C. Fourment, F. Deneuville, D. Descamps, F. Dorchies, S. Petit, O. Peyrusse, B. Holst, and V. Recoules, *Experimental determination of temperature-dependent electron-electron collision frequency in isochorically heated warm dense gold*, Phys. Rev. B **vol. 89**, p. 161110, URL http://link.aps.org/doi/10.1103/PhysRevB.89.161110 (2014) 2.3, 2.3, 4.1, **??**, **??**

[6] H. Zhang, S. A. Wolbers, D. M. Krol, J. I. Dijkhuis, and D. van Oosten, *Modeling and experiments of self-reflectivity under femtosecond ablation conditions*, J. Opt. Soc. Am. B **vol. 32**, no. 4, pp. 606–616, URL http://josab.osa.org/abstract.cfm?URI=josab-32-4-606 (2015) 2.4, 3.3

[7] O. enabling innovative electronics, *Spin coating: A guide to theory and techniques*, URL http://www.ossila.com/pages/spin-coating, [Online; accessed 24-September-2015] (2014) 3.1

[8] M. Scholten, *Experiment on ablation of dielectrics on gold, and water*, Master's thesis, Utrecht University, the Netherlands (2016) 3.2.1, 3.2.2

[9] M. W. Davidson and M. Abramowitz, *Optical microscopy*, URL http://www.olympusmicro.com/primer/microscopy.pdf 3.3

[10] N. D. Kosters and D. van Oosten, *Isolation of single gold nanoparticles* (2014) 3.3

[11] J. Findley de Regt, *Effect of damping on stability of gold nano-spheres in a quadrupole trap*, Master's thesis, Utrecht University, the Netherlands (2016) 3.3

[12] Z. Lin and L. Zhigilei, *Electron-phonon coupling and electron heat capacity in metals at high electron temperatures*, URL http://www.faculty.virginia.edu/CompMat/electron-phonon-coupling, [Online; accessed 23-May-2016] (2012) 4.1.1, 4.2, **??**

[13] J. Hook and H. Hall, *Solid State Physics*, John Wiley & Sons (2010) 4.1.1

[14] C. F. Bohren and D. R. Huffman, *Absorption and scattering of light by small particles*, URL `https://cds.cern.ch/record/110974`, reprint by Wiley in 2004 (1983)